International Journal of Machine Tools & Manufacture 118–119 (2017) 73–90

Contents lists available at ScienceDirect

International Journal of Machine Tools & Manufacture

journal homepage: www.elsevier.com/locate/ijmactool

Laser powder bed fusion of Ti-6Al-4V parts: Thermal modeling and mechanical implications

Mohammad Masoomi, Scott M. Thompson*, Nima Shamsaei

Laboratory for Fatigue & Additive Manufacturing Excellence (FAME), Department of Mechanical Engineering, Auburn University, Auburn, AL 36849, USA

ARTICLE INFO

Keywords:
Additive manufacturing
Multi-laser
Selective laser melting
Residual stress
Microstructure
Simulation

ABSTRACT

A continuum-scale modeling approach is developed and employed with three-dimensional finite element analysis (FEA), for simulating the temperature response of a Ti-6Al-4V, two-layered parallelepiped with dimensions of $10\times5\times0.06$ mm^3 during Laser Powder Bed Fusion (L-PBF), a metals additive manufacturing (AM) method. The model has been validated using experimental melt pool measurements from the literature and also accounts for latent heat of fusion and effective, temperature-dependent transport properties. The discretized temperature, temperature time rate of change (i.e. cooling rate) and temperature gradient are investigated for various scan strategies and number of lasers, i.e. 1, 2 or 4. The thermal response inherent to multi-laser PBF (ML-PBF) is investigated. The number of sub-regional areas of the powder bed dedicated to individual lasers, or 'islands', was varied. The average, maximum cooling rate and temperature gradient per layer, as well as the spatial standard deviation, or uniformity, of such metrics, are presented and their implications on microstructure characteristics and mechanical traits of Ti-6Al-4V are discussed. Results demonstrate that increasing the number of lasers will reduce production times, as well as local cooling rates and residual stress magnitudes; however, the anisotropy of the residual stress field and microstructure may increase based on the scan strategy employed. In general, scan strategies that employ reduced track lengths oriented parallel to the part's shortest edge, with islands 'stacked' in a unit-row, proved to be most beneficial for L-PBF.

1. Introduction

Additive manufacturing (AM) is an appealing means for generating complex-shaped, metallic components conformal to specific applications. A metallic feedstock, typically in the form of powder or wire, is processed to generate a target volume from the ground-up using solid model data, directed energy, computer numerical control (CNC) and an inert or evacuated atmosphere. Many industries, ranging from aerospace to biomedical, have taken interest in employing AM for production of application-tailored components [1,2]; however, before such parts can be used reliably, their quality and mechanical strength must be verified and assured [3–5]. By determining 'feedstock-process-property-performance' relationships inherent to a specific material/feedstock and process, such efforts can be expedited. Since the macro/microstructure of many metallic AM parts is directly coupled with the heat transfer experienced during their manufacture, process-property relationships can be elucidated by observing and quantifying part temperature and other thermal phenomena during its AM.

Powder Bed Fusion (PBF) is an AM method used for fabricating metallic (or ceramic) components via directed energy and a pre-deposited layer (or 'bed') of powder feedstock [6]. The energy source can be in the form of a focused electron beam or laser. When a laser is used as the energy source, the process is referred to as Laser-PBF (L-PBF). The localized laser irradiation results in a very high heat flux that overcomes powder latent heat of fusion, forming a micro-sized pool of molten material; i.e. the melt pool. As the laser beam moves away from the irradiated location, the melt pool solidifies very rapidly, forming a track of solid material. This process is repeated to form multiple tracks within a single layer based on a user-defined laser scan (or scanning) strategy. Upon finishing the build, the structure is detached from the substrate and excess powder is removed. In general, the PBF part will possess a net shape due to partially melted powder along its surface. Post-PBF, subtractive machining procedures are often employed for achieving target surface quality and tolerances.

A schematic of the L-PBF process is shown schematically in Fig. 1. A moving laser, melt pool, powder bed, part, substrate and a recently solidified track are depicted, as well as all modes of local heat transfer, i.e. conduction, convection and thermal radiation. The heat transfer process is initiated upon the selective laser irradiation of the pre-deposited powder bed. The solid region in the neighborhood of the melt

* Correspondence to: Department of Mechanical Engineering, 1418 Wiggins Hall, 354 War Eagle Way, Auburn, AL 36849.
E-mail address: smthompson@auburn.edu (S.M. Thompson).

http://dx.doi.org/10.1016/j.ijmachtools.2017.04.007
Received 11 February 2017; Received in revised form 12 April 2017; Accepted 13 April 2017
Available online 14 April 2017
0890-6955/

Nomenclature

AMCR	average maximum cooling rate, °C/s
AMTG	average maximum temperature gradient, °C/μm
c	specific heat capacity, J/kg K
C	heat capacity, J/K
d	diameter, m
F_o	view factor
G	laser heat flux, W/m^2
h	heat transfer coefficient, W/m^2 K
k	thermal conductivity, W/m K
Δl	layer height thickness, m
L	latent heat of fusion, kJ/kg
n	normal direction outward to surface
P	laser power, W
P	number of islands
Pr	Prandtl number
q	heat flux, W/m^2
q	heat flux vector, W/m^2
R	effective laser beam radius, m
Re	Reynolds number
SDCR	standard deviation of average maximum cooling rate, °C/s
SDTG	standard deviation of average maximum temperature gradient, °C/μm
T	temperature, K or °C
$T_{i,o}$	temperature at previous time step, K or °C
t	time, s
Δt_M	time elapsed between each layer, s
t_{step}	time step, s
V	volume, m^3
v	laser scanning velocity, m/s
W	track length, m
x	spatial ordinate, m
y	spatial ordinate, m
z	spatial ordinate, m

Greek

α	total/spectral absorptance
ε	emissivity
γ	kinematic viscosity, m^2/s
Γ_m	mass fraction function
Π	rectangular function, s
ϕ	powder bed porosity
ρ	density, kg/m^3
σ	Stefan-Boltzmann constant, W/m^2 K^4
τ	absorption coefficient, cm^{-1}
θ	solid-phase volume fraction

Subscripts

c	cooling
conv	convection
eff	effective
g	gas
h	heating
l	liquid
las	laser
mp	melt pool
pb	powder bed
rad	radiation
s	solid
surr	surroundings

pool is the heat affected zone (HAZ). A portion of the incident energy delivered from the laser, typically at constant wavelength, is absorbed and this ratio of energy, or absorptivity, depends on powder surface properties which are dictated by its phase (solid or liquid), temperature, cleanliness, oxidization, material type, shape, etc. Absorbed thermal energy is primarily used for melting the powder by overcoming its latent heat of fusion. Thermal energy not used for melting is utilized for sensible heating of the melt pool, surrounding solidified tracks and/or powder bed [7,8]; evaporation of the melt pool can also occur [9,10]. The non-isothermal melt pool can circulate due to density and surface tension gradients [11], and local mass transfer is also possible [12]. The high heat fluxes inherent to L-PBF allow parts to experience localized, extreme temperature gradients near their HAZ and highly-dynamic, as well as high magnitude, heating/cooling and solidification rates during their manufacture [9,10]. These temperature gradients and cooling rates can result in adverse material side effects such as residual stress or pore/defect formation, respectively [13,14]. Due to cyclic, laser-induced conduction with previously-deposited layers and adjacent tracks, the microstructure of the part continues to evolve even after its initial solidification. Cooling rates are driven by conduction through the HAZ, as well as heat loss to the process/shielding gas and enclosure walls via convection and thermal radiation, respectively.

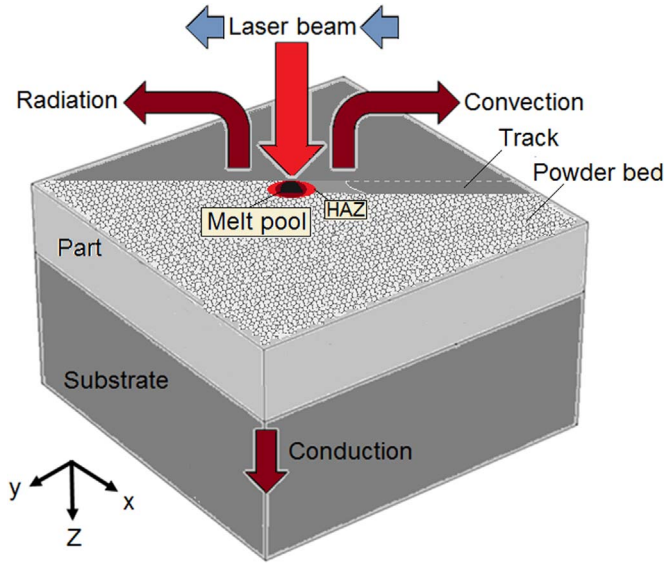

Fig. 1. Schematic of a typical L-PBF process consisting of a single moving laser beam, powder bed, solidified tracks, part and substrate. The modes of heat transfer in proximity to the melt pool and HAZ are shown.

Many free L-PBF (and PBF in general) process parameters exist, including: laser power, laser heating area, scan speed, inter-layer time interval, and hatching distance. There are also free design parameters, such as type of material, laser scanning pattern, build orientation, powder size, powder distribution and more. Utilization of various process/design parameter combinations results in a part possessing a unique spatiotemporal temperature field, or thermal history, during fabrication. Since thermal history directly affects the microstructure, residual stress and pore/defect distribution within L-PBF parts, its quantification allows one to better select process/design parameters for a desired quality tolerance and microstructure. This is the motive for understanding process-property relationships inherent to L-PBF.

If an operator aims to minimize the variation in PBF process parameters throughout a build, quality control is perhaps easiest achieved by strategically determining optimal scan patterns a priori, such that adverse thermal effects associated with part size, geometry

and complexity are minimized. Such scan patterns are at the full discretion of the part designer/manufacturer and implementable on a per-layer basis. A part layer can be built on a sub-regional basis, each with a dedicated scan path, in a specific sequence; or the entire layer can be built using a single scan path that 'sweeps' across the layer in a single direction. Each sub-region, or 'island', can possess its own laser scan sweep direction. Many possible options exist for island division per layer and path strategy per island, as well as for the island formation sequence per layer (i.e. order in which islands are solidified). Recent work has demonstrated that island scan strategies are effective in reducing residual stress within PBF parts [15,16].

Due to the locality and speed of fusion during L-PBF, residual stress formation within the fabricated materials can be high. Various residual stress distributions within the part can lead to delamination [17], as well as observable geometric intolerances, such as bowing or warping [18]. The HAZ temperature field conducive to residual stress formation is typically characterized by highly-localized, spatial variation in temperature, i.e. temperature gradients in HAZ, and/or the rapid temperature time rates of change. For PBF [18–22] residual stress can be mitigated via proper support structuring at the part/substrate interface and/or assigning more appropriate laser scan directions per layer; appropriate scan planning has found to mitigate residual stress in parts fabricated via Directed Energy Deposition (DED) methods, as well [23]. Parry et al. demonstrated via thermo-mechanical simulation that residual stresses in PBF parts are anisotropic due to non-uniform thermal history and typically increase with longer tracks [21]. Hussein et al. [24] numerically demonstrated, for the L-PBF of stainless steel (SS) 316 L, that temperature gradients are highest at the beginning of each track and subsequently decrease along track length. Nickel et al. [25] and Cheng et al. [26] demonstrated, via simulation of the PBF process, that the use of islands with scan paths that vary in direction for each new layer (i.e. rotating directions) can result in parts possessing more uniform residual stress distributions.

Kruth et al. [27] experimentally studied the effects of scan direction on part temperature gradients during L-PBF of Ti-6Al-4V. Shorter scan vectors, or tracks, were found to result in the part experiencing smaller temperature gradients and thermal stress. It was also found that preheating the substrate generally reduces intra-part temperature gradients during manufacture. In another study, Kruth et al. [28] fabricated parts with dimensions of $35\times15\ mm^2$ from iron-based powder via four different scan patterns. Two patterns consisted of the laser moving along the regular X and Y directions; while the other two scan patterns employed 21 islands, each $5\times5\ mm^2$, or 42 islands, each $2.5\times2.5\ mm^2$. The results suggested that samples fabricated using an island-based scan strategy deformed less relative to samples fabricated with no sub-regions/islands (i.e. one 'island'). Nickel et al. [25] made similar conclusions via finite element methods and numerical simulation.

Thijs et al. [29] studied the effects of scan strategies on the microstructure of AlSi10Mg and found that part texture can be controlled by rotating the scanning direction 90 ° between neighboring islands for a given layer. Lu et al. [30] built $10\times10\times10\ mm^3$ Inconel 718 parts using L-PBF while employing an island-based scan strategy consisting of various island sizes. It was found that scan strategies employing larger islands resulted in parts having higher density, while microstructure, ultimate tensile strength, and yield strength demonstrated only a slight dependence on the number of islands employed. The residual stress within the part was found to increase with island size. Bo et al. [31] studied the effects of swirl/helix-type scan patterns on the mechanical response of SS 316 L parts during L-PBF. Parts fabricated using this scan pattern were found to possess a relatively rougher surface consisting of ravines between tracks. Part dimensional accuracy was also found to be less relative to parts fabricated using unidirectional scan patterns. Li et al. [18] demonstrated that part distortion in the laser scan direction is lowest relative to other directions, and that using island scan strategies can result in decreased deformation of the final part. Bending of the part away from the substrate, in the height-wise direction, was also reported as the most prevalent form of distortion for the unidirectional scan strategies investigated.

Since the typical PBF process employs a relatively small directed energy area, powder size, and layer thickness, and due to the fact that many PBF machines takes time to deposit/remove powder for each new layer ('coating' procedure and post-fusion clean-up), today's PBF process can take multiple hours to complete [32], and this provides a challenge to manufacturers targeting fast production rates. Further, in a typical PBF process, each new powder layer is 'over-sized' and spans the entire width and length of the chamber, and this can add significant time to production of small-sized parts. Hence, in order for the PBF process to be more attractive for high volume production, in terms of both component size and quantity, it is of interest to decrease the time associated with part manufacture. One solution is to employ multiple directed energy sources; allowing the cross-sectional geometry of the part to be divided into individual islands each possessing their own dedicated directed energy source. In this way, parts can be fabricated by densifying multiple islands in parallel, with each island having its own scan strategy and build sequence. The directed energy source can be split (diffracted) or multiple energy sources [33–36] can be utilized. When multiple lasers are used to accomplish PBF, the process can be referred to as multi-laser PBF (ML-PBF).

A potential challenge for ML-PBF lies in the fact that using multiple islands may impact the quality of manufactured parts. As shown for single-laser PBF, such island strategies can introduce porous/unmelted regions concentrated between islands [30,37]. In addition, the effective scan strategies for ML-PBF, and the degree in which such strategies deviate from those used for single-laser PBF, have not been clearly identified. Hence, this study aims to elucidate relationships between scan strategies and mechanical properties of Ti-6Al-4V for both single and multi-laser PBF for aiding process and product design decisions. Although the use of multiple lasers during welding and cladding has been investigated [32,38–41], the effects of ML-PBF on material properties and residual stress still needs attention.

Since determination of the appropriate scan strategy for ML-PBF can be challenging, as more free design/process variables are introduced, the problem herein is reduced to synchronous, orthogonal multi-laser scan strategies. The ML-PBF process is modeled and then simulated for various scan strategies as to determine effects of laser number, scan pattern and part size on the spatiotemporal temperature distribution of Ti–6Al–4 V material during its first few layers of densification. Titanium alloy is selected for demonstration purposes only, while the model is applicable to various other materials. Ti-6Al-4V has commercial appeal in various industries, including chemical [42] and biomedical [43], and its microstructure is relatively sensitive to cooling rate [44], allowing it to be a suitable material for consideration herein.

2. Physical model

The transient heat transfer during the L-PBF of metals is complex; exhibiting dense heat flux transport, inhomogeneous phase change, short length/time scales, melt pool instability, surface/fluid interaction, microstructural coupling, anisotropic microstructural growth and more [3,45]. Utilizing a physical model that reduces this complexity can be advantageous for minimizing computational investment and for providing general insight into the process-property relationships inherent to parts fabricated via PBF. One such approach is to model the heat diffusion in all participating media while neglecting, or creatively accounting for, secondary/tertiary effects such as melt pool flow dynamics, powder bed mechanics, powder heterogeneity and microstructural evolution (i.e. solid-phase transformations). Then, the melt pool, powder bed and solidified part may be represented as continua with effective density and transport properties, and this

approach is adopted herein.

As shown in Fig. 1, all modes of heat transfer, i.e. conduction, convection and thermal radiation are present during L-PBF. For modeling purposes, melt pool convection and phase-change can be accounted for by employing an effective melt pool thermal conductivity and by estimating the latent heat transfer due to melting. More advanced solidification phenomena such as solid-phase nucleation, liquid-solid wetting behavior, pore generation, and more, can be neglected while understanding that the predicted temperature response is only an estimation. Such temperature response provides insight to the process-property relationships for that given material.

For the sake of mathematical formulation, and in an attempt to formalize scan planning, a simplified ML-PBF process is described. This particular process involves the manufacture of a rectangular part with uniform cross-sectional area and single material type; fabricated using P identical lasers (i.e. same wavelength, intensity profile, etc.), each operating at the same scan speed and power. Each laser may have its own scan strategy and, any group of lasers are assumed to not intersect, operate synchronously (i.e. starting and ending at the same time) and have time-invariant power and scan speeds. Consistent with literature to date, the region of the powder bed dedicated to a single laser scan pattern is referred to as an 'island', J. Islands are constrained to have rectangular shapes distributed along a layer uniformly.

Each layer consists of $J \geq 1$ identical islands, and each island may consist of $K \geq 1$ identical sub-islands built sequentially by each island-dedicated laser. An island is defined as a sub-region dedicated to a single laser, while a sub-island is defined as a sub-region within an island dedicated to the same laser; hence, $P = J$ herein. The number of sub-islands per island follows the rule: $K \geq J$ and the number of sub-islands for each island is assumed constant. Sub-islands may consist of sub-islands, and so forth, indefinitely; however, these scenarios are not examined in this study. One may quantify the 'order' of island division on a per layer basis using a 'level of island planning' (LIP) metric which describes the number of lasers and the parallelism of island building. A LIP of zero order, i.e. LIP-0, indicates that the entire powder bed functions as a single island and that a single laser is used (i.e. $J = K = 1$), a LIP-1 indicates sequenced, sub-island scanning for a single laser (i.e. $J = 1$, $K > 1$), a LIP-2 indicates 'all at once' ML-PBF, in which a layer is divided into separate islands with 1 sub-island per island (i.e. $J > 1$, $K = 1$), finally, a LIP-3 indicates that the powder layer is divided into islands that consist of sub-islands, to be built in a prescribed sequence, per island (i.e. $J > 1$, $K > 1$). An individual layer may be fabricated on an island-by-island basis with a single laser, i.e. in-series island building corresponding to LIP-1 (single laser) or LIP-3 (multi-laser), or with all islands built at once, i.e. in-parallel island building, corresponding to LIP-0 (single laser) or LIP-2 (multi-laser). An aerial view of the ML-PBF domain, for an arbitrary case of $P = J = K = 4$, is shown schematically in Fig. 2.

The LIP for each layer of powder requires a description of the island division scheme (IDS), which indicates how sub-islands and islands are divided. One can impose an IDS with the aid of island border lines as shown in Fig. 2. Herein, these border lines are constrained to be collinear with the edges of the part. In addition, a uniform IDS is employed such that all islands (and sub-islands) have identical area. The number of lasers used per layer does not necessarily have to equal the number of lasers available; in general, each laser must be assigned specific islands for each new layer. For instance, a laser may have a different angle-of-attack, intensity and/or wavelength more desirable for a given island in some cases. The laser assignment per layer follows a matrix $\boldsymbol{J}_P$ where each island is labeled.

Each sub-island, consisting of $N \geq 1$ tracks, consists of a scan plan that dictates laser motion during its fabrication. If the rectangular part consists of M, equal-LIP layers of height, Δl, then the final part consists of M x J x K x N total tracks. Herein, scan plans are constrained to form tracks collinear with the width (x) and/or length (y) of the layer. Note that the general direction in which tracks are added (i.e. perpendicular to tracks) is referred to as the track sweep direction. For in-series PBF, i.e. LIP-1 and LIP-3, the sub-island sequence or order must be specified. The employed L-PBF/ML-PBF process then consists of a per-layer build plan consisting of the: LIP, IDS, laser-to-island assignments and sub-island scan plans.

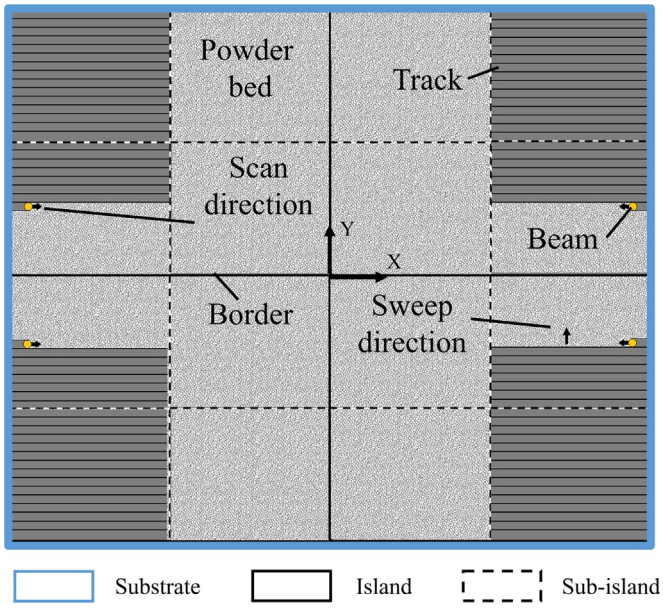

Fig. 2. Aerial view of a LIP-3 ML-PBF process for building a single part atop a powder bed while employing a scan strategy involving four islands (J =4), 4 sub-islands per island (K =16) and four synchronized lasers (P=4). The island/sub-island borders and track scan/sweep directions are also shown.

Absolute temperature, T_i, within bounded i^{th} continuum region, which may be the solid phase (part), liquid phase, mixed solute phase (i.e. mushy zone), or powder bed, abides conservation of energy for a given time, t_0, i.e. Eq. (1), during the selective laser irradiation of arbitrary layer M, i.e.:

$$\rho c_i(T_i)\big|_{t_o-\Delta t}\left.\frac{\partial T_i(x,\,y,\,z,\,t)}{\partial t}\right|_{t_o} = \nabla k_i(T_i)\big|_{t_o-\Delta t}\left.\nabla T_i(x,\,y,\,z,\,t)\right|_{t_o} \quad (1)$$

where c_i is specific heat capacity and k_i is continuum thermal conductivity. The continua distribution/phase during L-PBF is coupled with the unknown temperature field; therefore, it is evaluated at a previous time, t_0-Δt, and updated based on local temperature, T_i. Temperature gradients at the boundaries of each continuum region are assumed differentiable. The x-z and y-z planes of island borders in contact with the edge of the build chamber are assumed insulated, while interior island borders are assumed to have zero interfacial thermal resistance. Note that the process of adding more powder to the PBF build chamber results in elapsed time, Δt_M, between the final sinter(s) on layer $M-1$ and the start of laser scanning on layer M.

The rate of energy delivered by the laser ensemble is either used for quickly overcoming the latent heat of fusion of powder for melting, q_{melt}, or transferred via conduction through the melt pool, $\boldsymbol{q}_{mp}$, gas-entrapped powder, $\boldsymbol{q}_{pb}$, or non-powder solid material (i.e. built part), $\boldsymbol{q}_s$. Heat exchange also occurs with the surroundings via thermal radiation, $q_{rad,net}$, and/or convection, $q_{conv,net}$. Thermal radiation between melt pools and neighboring islands is neglected. For a given time and control surface atop an arbitrary layer, M, atop the J^{th} island, the energy balance can be represented as:

$$q_j - q_{melt} = \left\|\boldsymbol{q}_{pb}\right\| + \left\|\boldsymbol{q}_s\right\| + \left\|\boldsymbol{q}_{mp}\right\| + q_{conv,net} + q_{rad,net} \quad (2)$$

where q_j is the island surface heat flux due to laser irradiation. With respect to a growing control volume, $V_t(t)$, that encapsulates the entire part and powder bed, and by accounting for the phase change heat

transfer within the melt pool via an effective specific thermal capacitance, the heat exchange between the total volume and surroundings is conserved following:

$$\iint_{A_{c,pb}}\left(Pq_j - q_{conv,net} - q_{rad,net}\right)dA_{c,pb} \cong \iiint_{V_i(t)}\rho_i(T_i)c_i(T_i)\frac{\partial T_i(x,\,y,\,z,\,t)}{\partial t}dV_i(t) \tag{3}$$

where $A_{c,pb}$ is the initial, exposed cross-sectional area of the powder bed.

The laser position relative to the imposed coordinate system, (x, y), as dictated by the scan strategy/path assigned to each island, $X_J(t)$, results in a temporal heat flux distribution at the exposed boundary of each island. The laser power absorbed by the melt pool and surrounding powder is assumed to have a Gaussian intensity profile. As a result, each laser-sourced heat flux penetrates through the melt pool and powder bed following:

$$q_{laser}(X_j(t),\,z) \cong \alpha_\lambda\frac{2P}{\pi R^2}\exp\left(-\frac{2[(x-x_c)^2+(y-y_c)^2]}{R^2}\right)I(z) \tag{4}$$

where α_λ is the hemispherical, spectral (at λ=1040 nm) absorptance of the irradiated, two-phase powder bed region, R is the effective laser beam radius at which intensity reduces to the constant $1/e^2$, and (x_c, y_c) is the laser spot center location [46]. The absorptance corresponding to irradiation of the melt pool is assumed to be temperature independent and near-equal to that of the solid part and powder during the heating and cooling processes [47,48], i.e.: $\alpha_\lambda \cong \alpha_{pb} \cong \alpha_{mp} \cong \alpha_s$. Laser energy is assumed to transmit through the melt pool and adjoining powder via Beer-Lambert attenuation [49], $I(z)$, i.e.:

$$I(z) = \exp(-\tau_\lambda(z + M\Delta l)) \tag{5}$$

where τ_λ is the absorption coefficient of the irradiated region.

During L-PBF, temperature variation within the powder bed and part drives non-uniform conduction of various, local magnitude and direction through various continua. Due to the ultra-high heat flux delivered by each laser, significant temperature gradients exist due to thermal spreading resistance [50] in vicinity of the superheated melt pool, i.e. within the powder bed, previous layers, neighboring tracks and substrate. Via Fourier's law, these temperature gradients, combined with an effective thermal conductivity, define a local heat flux vector within the powder bed, $\boldsymbol{q}_{pb,i}$, superheated melt pool, $\boldsymbol{q}_{mp,i}$, and surrounding (non-powder) solid media, $\boldsymbol{q}_{s,i}$, i.e.:

$$\boldsymbol{q}_{pb,i} = -k_{pb}|_{T_{pb,i}}\nabla T_{pb} \tag{6}$$

$$\boldsymbol{q}_{mp,i} = -k_{mp}|_{T_{mp,i}}\nabla T_{mp} \tag{7}$$

$$\boldsymbol{q}_{s,i} = -k_s|_{T_{s,i}}\nabla T_s \tag{8}$$

The effective thermal conductivity of the powder bed, k_{pb}, is calculated for a given $T_{pb,i}$ using [51]:

$$\frac{k_{pb}}{k_g} = (1-\sqrt{1-\phi})\left(1+\frac{\phi k_r}{k_g}\right) + \sqrt{1-\phi}\left\{\frac{2}{1-\frac{k_g}{k_s}}\left[\frac{1}{1-\frac{k_g}{k_s}}\ln\left(\frac{k_s}{k_g}\right)-1\right] + \frac{k_r}{k_g}\right\} \tag{9}$$

where k_g is the thermal conductivity of the entrapped gas (e.g. argon), and ϕ is the porosity of the powder bed, i.e.:

$$\phi = \frac{\rho_s - \rho_p}{\rho_s} \tag{10}$$

The effective thermal conductivity of the irradiated powder, k_r, which depends on thermal radiation exchange between neighboring particles and the powder distribution/size [51], is found using:

$$k_r|_{T_{i,o}} = 4F_0\sigma T_{i,o}^3 d_p = \frac{4\varepsilon\sigma T_{i,o}^3 d_p}{1 - 0.132\varepsilon} \tag{11}$$

where F_o is the radiation view factor, σ is the Stefan-Boltzmann constant, d_p is the mean powder diameter and ε is the constant emissivity for a typical, spherical powder arrangement [51]. The effective thermal conductivity of the melt pool, k_{mp}, is estimated using:

$$k_{mp}|_{T_{mp,i}} = (1-\theta)k_{l,eff} + \theta k_s|_{T_{mp,i}} \tag{12}$$

where θ is the solid-phase volume fraction during melt pool formation; varying between 0 and 1, i.e.:

$$\theta = \frac{V_s}{V_s + V_l} = \frac{V_s}{V_{mp}} \tag{13}$$

and $k_{l,eff}$ is an effective, temperature-independent liquid thermal conductivity that accounts for heat transfer due to Marangoni and natural convection within the superheated melt pool [52,53]. Evaporation heat transfer within the melt pool is neglected herein.

Each continuum is assigned its own temperature-dependent specific thermal capacitance, c_i, relating heat flux to temperature rise. For the case of the melt pool, which is a mixed-phase alloy, an effective specific thermal capacitance, $c_{mp,eff}$, is defined for relating heat flux to both temperature rise and phase change. The effective melt pool specific thermal capacitance considers melt pool regions exceeding sintering temperature, T_s, and below melting temperature, T_m, found using:

$$\rho_{mp}c_{mp,eff}|_{T_{mp,i}} = [(1-\theta)\rho_l c_l + \theta\rho_s c_s] + \rho_{mp}c_L\Big|_{T_{mp,i}} \tag{14}$$

where melt pool density, ρ_{mp}, is found using:

$$\rho_{mp}\Big|_{T_{mp,i}} = (1-\theta)\rho_l|_{T_{mp,i}} + \theta\rho_s|_{T_{mp,i}} \tag{15}$$

and the effective latent heat capacity is approximated by:

$$c_L|_{T_{mp,i}} = L\frac{d\Gamma_m(\theta)}{dT} \tag{16}$$

where Γ_m is the mass fraction function defined as:

$$\Gamma_m = \frac{1}{2}\frac{(1-\theta)\rho_l - \theta\rho_s}{\theta\rho_s + (1-\theta)\rho_l} \tag{17}$$

Note that the mass fraction function equals −0.5 before phase change and 0.5 afterwards. Total thermal energy released during phase transformation, between solid and liquid, is then:

$$L|_{T_{mp,i}} = \int C_L|_{T_{i,o}}dT_{mp} \tag{18}$$

The specific thermal capacitance of the powder bed is found using:

$$c_{pb}|_{T_{pb,i}} = (1 - \varnothing)c_s|_{T_{pb,i}} \tag{19}$$

where c_s is the specific thermal capacitance of the solid phase material.

Heat transfer via convection and thermal radiation, between exposed continua and surroundings, is estimated by assuming that exposed portions of the powder bed and part possess an average temperature, $\overline{T}_{pb}$, for the M^{th} layer, and that the shielding gas and chamber walls are at a uniform, constant temperature, T_∞, i.e., for convection:

$$q_{conv,net} = \overline{h}(\overline{T}_{pb} - T_\infty) \tag{20}$$

with:

$$\overline{T}_{pb} = \frac{1}{A_{c,pb}}\iint T_i(x,\,y,-m\Delta l,\,t)dA_{c,pb} \tag{21}$$

where all fluid properties are evaluated using a film temperature, $T_f = (\overline{T}_{pb} + T_\infty)/2$. Convection between the exposed powder bed and chamber gas is assumed uniform and forced with a total heat transfer coefficient, $\overline{h}$; depending on chamber gas speed (near surface),

u_∞, and inert gas properties [54], i.e.:

$$\bar{h} \cong \frac{k_g}{W}\frac{0.6774 \mathrm{Re}_L^{1/2}\mathrm{Pr}^{1/3}}{\left[1+\left(\frac{\mathrm{Pr}}{0.0207}\right)\right]} \tag{22}$$

with

$$\mathrm{Re}_L = \left.\frac{u_\infty W}{\gamma_g}\right|_{T_f} \tag{23}$$

where γ_g is the gas kinematic viscosity, Re_L is the gas Reynolds number, Pr is the gas Prandtl number and W is the width of the powder bed (i.e. along Y direction). Thermal radiation between the exposed powder bed area and surrounding chamber walls is calculated using:

$$q_{\mathrm{rad,net}} = \sigma\varepsilon_{\mathrm{pb}}(\bar{T}_{\mathrm{pb}}^4 - T_\infty^4) \tag{24}$$

where $\varepsilon_{\mathrm{pb}}$ is the average powder bed thermal emissivity.

3. Numerical methodology and validation

3.1. Numerical methodology

The spatiotemporal temperature field encompassing the substrate, powder bed, solidified part and melt pool was estimated by discretizing and numerically solving Eq. (1) via finite difference. Since the L-PBF process consists of phase change and energy transport occurring at relatively fine spatial and temporal scales, e.g. micrometers and microseconds, respectively, highly resolved discretization of the energy equation was sought. A 3072 core cluster setup was utilized to expedite the simulation process while maintaining a fair level of accuracy. Simulations were performed using the commercially- available software COMSOL Multiphysics® 5.1 in conjunction with custom coding scripts.

For all simulations, a tetrahedral meshing scheme consisting of uniform grid spacing with respect to the Z-direction was employed for discretization of the continuum powder bed, part and substrate. As shown schematically in Fig. 3, a mesh with finer spatial resolution was employed for all layers of the powder bed inspected; while a mesh with less spatial resolution was imposed for the substrate. Finer, intra-layer meshes typically consisted of cells with length approximately ~33% that of the laser diameter and a volume of approximately 230,000 μm^3; while coarser, intra-substrate meshes consisted of cells with 200% larger volumes. Deposition and spreading of powder atop the substrate and previously-processed layers was simulated by allowing finite time to pass between the last sinter and first sinter of the next layer (10 s). Fresh powder, with an initial temperature of T_∞, was assumed to be added instantaneously after the inter-deposit time elapsed. The new powder layer, as well as all previous layers and solid media (including substrate), were then subsequently meshed. An 'active cell' method was employed [55]; meaning, a new layer was activated as needed during simulation. Time was discretized into equal time steps of $\Delta t = 600$ μs.

Eq. (1) was solved for the discretized temperature distribution along the current layer and previous layer (or substrate) in response to the L-PBF of a multi-track/two-layer parallelepiped. Elements exposed to a laser beam were assigned a heat flux distribution and such elements were determined at each time step based on assigned scan paths. Properties of each element were assigned based on its continuum type as governed by element temperature for time, t_0, i.e.:

$$k_i(t_0) = \begin{cases} k_{\mathrm{pb}}, & T<T_s \\ k_{\mathrm{mp}}, & T_s<T<T_m \\ k_{\mathrm{eff,l}}, & T_m<T \\ k_s, & \forall t, T>T_m,\ T(t_0)<T_s \end{cases} \tag{25}$$

$$C_i(t_0) = \begin{cases} C_{\mathrm{pb}}, & T<T_s \\ C_{\mathrm{mp,eff}}, & T_s<T<T_m \\ C_l, & T_m<T \\ C_s, & \forall t, T>T_m,\ T(t_0)<T_s \end{cases} \tag{26}$$

Since the local temperature gradient consists of three spatial components, i.e. parallel-to-track (X), perpendicular-to-track (Y) and normal-with-substrate (Z) directions, the magnitude of local temperature gradients was calculated herein. The magnitude of the temperature gradient (for a given time) between neighboring elements separated by $<\Delta x, \Delta y, \Delta z>$ was estimated using a second-order central difference, i.e.:

$$\|\nabla T\| \cong \left\| \left\langle \frac{T(x+\Delta x,y,z)-T(x-\Delta x,y,z)}{2\Delta x}, \frac{T(x,y+\Delta y,z)-T(x,y-\Delta y,z)}{2\Delta y}, \frac{T(x,y,z+\Delta z)-T(x,y,z-\Delta z)}{2\Delta z} \right\rangle \right\| \tag{27}$$

The local temperature time rate of change, i.e. the heating or cooling rate at a given point, was estimated using:

$$\frac{\partial T_i}{\partial t} \cong \frac{T_i(t+\Delta t) - T_i(t)}{\Delta t} \tag{28}$$

3.2. Validation

The numerical model was validated by first simulating the thermally-monitored (via CCD camera) L-PBF process described by

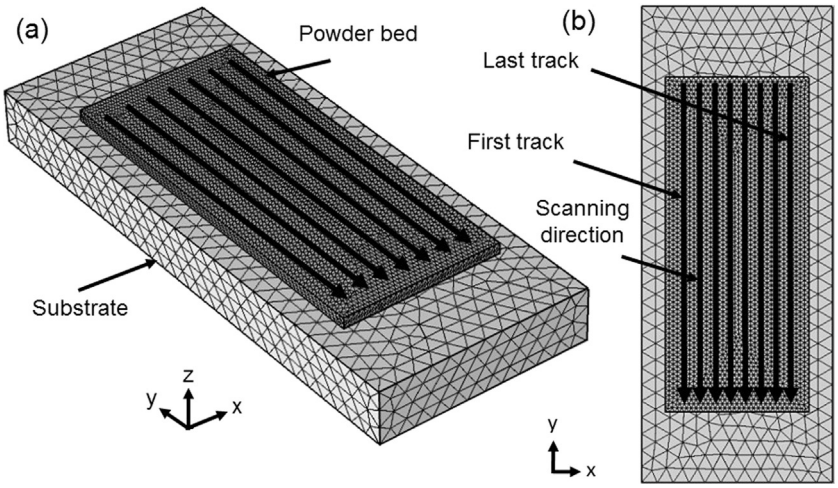

Fig. 3. Schematic of the meshing scheme used for numerical simulation with a layer of powder, substrate and unidirectional, length-wise scan pattern shown: (a) isometric and (b) aerial perspectives.

Yadroitsev et al. [56]. This study is of particular interest since it reports a representative Ti-6Al-4V melt pool temperature for various laser powers during typical L-PBF conditions. The system employed a ϕ =70 μm ytterbium fibre laser at 1075 nm wavelength with a Gaussian intensity profile. The substrate and the powder material were both Ti-6Al-4V. The substrate, which was not temperature controlled (i.e. not pre-heated), was assumed to possess dimensions of 100×100×10 mm^3. For a temperature measurement of 1873 K, the maximum error was reported as ± 25 K.

Temperature-dependent properties of solid and liquid Ti-6Al-4V [57] were employed and are shown as functions of temperature in Fig. 4. An effective melt pool liquid thermal conductivity between 25–45 W/m K [58] and a liquid/solid Ti–6Al–4 V absorptance of 0.25 [59] were assumed. Since the temperature gradient across the melt pool results in both density and surface tension variation that drives natural and Marangoni-type flows, respectively, the melt pool effective thermal conductivity should be higher, i.e. $k_{l,eff} > k_l$, due to convection effects. Since the fluid motion of the melt pool was not analyzed, and since an accurate melt pool thermal conductivity is currently unknown, it is assumed that $k_{l,eff} \approx k_l$. The temperature-dependent properties of argon were taken from [60].

The powder bed porosity was assumed to be 0.4 – typical of many L-PBF systems [21]. Laser power was varied between 20 W, 30 W or 50 W, while maintaining a scan speed of 100 mm/s. The L-PBF argon shielding gas flow rate was assumed to be 167 cm^3/s [7], providing a powder bed Reynolds number < 5E5 and therefore laminar flow conditions along the majority of the exposed powder bed surface. The characteristic heat transfer coefficient was found to be approximately 12.7 W/m^2 K. The initial temperature of the Ti–6Al–4 V powder bed and substrate was assumed to be 20 °C. The phase fraction of each cell, at each time step, was determined based on its relative location to the laser and its local temperature; thereupon, appropriate properties were assigned following the aforementioned procedures in Section 2. Details of the L-PBF process/design/system parameters employed by [56] and by the simulation herein are reported in Table 1.

The maximum melt pool temperature during L-PBF of a single track of Ti-6Al-4V, as predicted from the simulation, for laser powers of 20, 30 and 50 W, are compared with the maximum melt pool temperature measured experimentally by Yadroitsev et al. [56] in Table 2. It may be seen that the absolute relative error is less than 50 °C for the investigated calibration temperature of 1600 °C; being within the margin of error of the CCD (± 25 °C). The error between experimental and simulation results is found to not be strongly dependent on laser power.

The sensitivity of peak temperature to the layer-wise mesh size/resolution employed was inspected to ensure mesh-independent solutions. Following the approach detailed in Section 3.1, three mesh sizes, consisting of global maximum element sizes either 10% (Mesh #1), 33% (Mesh #2) or 100% (Mesh #3) of the laser diameter, were inspected. Laser power and speed was set at 50 W and 500 mm/s, respectively. The time interval was held constant at Δt = 500 μs, resulting in each laser moving 250 μm between each time step during simulation. The densification of a single, 10-mm-long track of Ti-6Al-4V powder material was simulated using parameters provided in Table 1. The difference between peak temperatures extracted from a point at the middle of the track was evaluated for different mesh sizes. This exercise demonstrated that track peak temperatures varied less than ~3% when using Mesh #3, and less than ~1% when using either Mesh #1 or Mesh #2. Therefore, in order to achieve sufficient solution accuracy with reasonable computational cost, spatial resolution associated with Mesh #2 was deemed sufficient as this particular study focuses more on relative differences in temperature for various build strategies and number of lasers. It should be noted that time was consistently discretized into equal time steps of Δt = 500 μs. Any solution-dependence on time discretization will increase as the laser speed increases.

Table 1
Parameters used for simulating the single-track L-PBF of Ti–6Al–4V as reported by Yadroitsev et al. [56].

Substrate material	Ti–6Al-4V [56]
Substrate size	10×10×1 cm^3
Powder description	Gas-atomized, air-dried [56]
Mean particle diameter	16.6 μm [56]
Powder layer thickness	50 μm [56]
Powder bed porosity	0.4
Laser spot diameter	70 μm [56]
Laser power	20 – 50 W [56]
Laser wavelength	1075 nm [56]
Scan speed	100 mm/s [56]
Powder bed absorptance	0.25 [59]
Absorption coefficient	10^6 cm^{-1} [49]
Emissivity	0.35 [51]
Melt pool liquid thermal conductivity	25 – 45 W/m K [56]
Shielding gas type	Argon [56]
Shielding gas temperature	20 °C
Shielding gas flow rate	167 cm^3/s
Chamber wall temperature	20 °C
Substrate temperature	20 °C
Convection heat transfer coefficient	12.7 W/m^2 K

Table 2
Experimentally-measured [56] and simulated maximum Ti-6Al-4V melt pool temperatures during single-track L-PBF for different laser powers at a scan speed of 100 mm/s.

Laser power (W)	References	Temperature (°C)
20	Experimental [56]	1650
	Simulation	1670
30	Experimental [56]	2050
	Simulation	2080
50	Experimental [56]	2340
	Simulation	2350

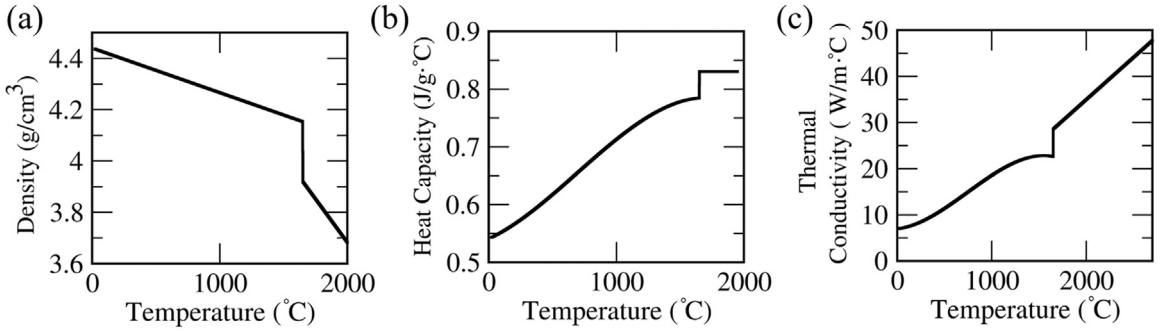

Fig. 4. Physical properties of solid- and liquid-phase Ti-6Al-4V versus temperature: (a) density (b) heat capacity and (c) thermal conductivity [57].

3.3. Simulations

The validated numerical model was used for simulating the ML-PBF of a Ti–6Al–4 V parallelepiped structure with dimensions of 10×5×0.06 mm^3 built using multiple tracks and consisting of two total layers. To present mechanically-relevant results, the parameters associated with the L-PBF process reported by Vilaro et al. [61], and summarized in Table 3, were utilized since they were proven effective in producing fully-dense Ti–6Al–4 V material. This particular study focused on fabricating tensile specimens via a Trumpf LF250 L-PBF system and no thermal monitoring was performed. As necessary, the validated numerical model employed parameters and constants (see Table 3) discussed earlier in Section 3.2; e.g. the melt pool liquid thermal conductivity, powder bed porosity, etc.

Using the parameters in Table 3, the L-PBF of an individual, two-layered parallelepiped was simulated for various laser numbers and scan strategies. Scan strategies were selected as to reduce overexposure of regions near island border lines; as some synchronous, multi-laser scan strategies can result in instances where all lasers are in close proximity thus affecting prediction accuracy. The number of islands and sub-islands were varied while track sweeping directions (i.e. X+ or Y+ directions) were held constant for all islands/sub-islands employed. The scan strategy was repeated for the first and second layers in all simulations conducted. In total, 13 different simulations, i.e. S1-S13, were performed, with S1-S5 employing a Y+ track sweep direction, S6-S10 employing a X+ track sweep direction and S11-S13 employing 'mixed' X+/Y+/X-/Y- track sweep directions.

Islands and sub-islands were built using a quadrant-, halves- or fourths-style IDS. For the quadrant division scheme, the part (or island) was divided into four equally-sized islands (or sub-islands) with division lines intersecting at the center of the part (or island). The sequence in which quadrants were built varied with number of lasers used. For P=1, the top-left quadrant, i.e. Q1, was fabricated and the next island manufactured was selected in a clockwise (cw) fashion, with the bottom-left quadrant being Q4, as shown in Fig. 5. The 'fourths' island division scheme allowed islands to be positioned adjacent to each other in a single row with X-parallel or Y-parallel division lines, while the 'halves' division scheme allowed for two islands formed by a Y-parallel division line. The part was also fabricated using no division scheme, i.e. a 'full' or 'single' island division. Fig. 5 illustrates the various scan patterns (SPs) investigated for: P=1, P=2, P=4; referred to now as SP-A, SP-B, and so forth, until SP-H, corresponding to Fig. 5(a)–(h), respectively. The various simulations performed with respect to the investigated scan patterns and division schemes/sequences are summarized in Table 4. The various scan patterns investigated are shown schematically in Fig. 5.

Simulation S1 employed SP-A and a single laser dedicated to a single island (i.e. LIP-0) with laser tracks swept parallel to the part's shortest edge in the Y+ direction. Simulation S2 employed the quadrant IDS and scan pattern SP-C while using a single laser swept in the Y+ direction for the in-series building of 4 sub-islands in the following clockwise sequence: Q1, Q2, Q3 and then Q4. Here, Q1-Q4 are the names of sub-islands as shown in Fig. 5. Simulation S4 is similar to S2 except that 4 lasers were used for in-parallel building of islands Q1-Q4 (i.e. LIP-2). Simulation S3, being a LIP-3 build plan, employed the halves IDS and scan pattern SP-C while using 2 lasers swept in the Y+ direction for the in-series building of 2 sub-islands per island in the following sequence: Q1 then Q4 in-parallel to Q2 then Q3. Simulation S5 employed the fourths IDS and scan pattern SP-F while using 4 lasers swept in the Y+ direction for the in-parallel building of 4 islands. Simulations S6-S10 followed the strategies detailed by S1-S5, respectively, except that scan patterns SP-B (for S6), SP-D (for S7-S9) and SP-G (for S10) were employed along with a X+ track sweep directions. Simulations S11-S13 employed the quadrant IDS and tracks with mixed sweep directions. Simulation S11 employed a single laser and scan pattern SP-E for the in-series building of 4 sub-islands in the Q1-Q4 sequence (LIP-1). Simulation S12 employed 4 lasers and scan pattern SP-E for the in-parallel building of 4 islands (LIP-2). Finally, S13 employed 4 lasers and scan pattern SP-H for the in-series building of 4 sub-islands per island; all sub-islands were built in the Q1-Q4 sequence (LIP-3).

Sixteen points, i.e. P1-P16, were imposed along each layer for extracting local temperatures, cooling rates and temperature gradients during simulations S1-S13. Each 'extraction point' was centered within a sixteenth of the parallelepiped volume as illustrated in Fig. 6. These temperature measurement/exaction points enabled a means to investigate local, transient behavior of the powder bed/part temperature distribution.

The real-time distances between lasers dedicated to Q2-Q4 relative to Q1 for S12 and S4 are shown in Fig. 7. This relative motion of island scan paths allows another means to understand measured thermal phenomena. For instance, it may be seen that the distance remains constant with time for S4 and S9 in which unidirectional island sweep directions are used, while it oscillates with time for S12, in which each island has a different laser track sweep direction. A constant or oscillating relative laser position during LIP >2 will affect the layer thermal response. Local temperatures will increase when lasers approach each other and their relative distance decreases. By keeping the laser distance constant between regions, the thermal response will be more homogenous.

Table 3
Parameters used for simulating the L-PBF and ML-PBF of a Ti–6Al–4V parallelepiped based on those reported by Vilaro et al. [61].

System	Trumpf LF250 [61]
Substrate material	Ti–6Al-4V [61]
Substrate size	10×10×1 cm^3
Powder description	Gas-atomized, air-dried [61]
Mean particle diameter	35 μm [61]
Powder layer thickness	30 μm [61]
Powder bed porosity	0.4
Hatch spacing	200 μm [61]
Laser spot diameter	220 μm [61]
Laser power	200 W [61]
Scan speed	500 mm/s [61]
Powder bed absorptance	0.25 [59]
Absorption coefficient	10^6 cm^{-1} [49]
Emissivity	0.35
Melt pool thermal conductivity	25 – 45 W/m K [58]
Shielding gas type	Argon
Shielding gas flow rate	167 cm^3/s
Shielding gas temperature	20 °C
Chamber wall temperature	20 °C
Convection heat transfer coefficient	12.7 W/m^2 K

4. Results and discussion

4.1. Temperature of melt pool and heat affected zone

The melt pool and HAZ temperature distributions, halfway through building the first layer, for S1, S4 and S5 are shown in Fig. 8(a) – (c), respectively; while a magnified view of a representative melt pool corresponding to S1 is provided in Fig. 8(a). The representative melt pool is found to be semi-circular with a maximum temperature zone possessing a diameter near that of the laser. The HAZ possesses a thermal 'wake' that follows behind the melt pool. Each laser produces identical melt pools and HAZs. As shown in Fig. 8, increasing the number of lasers increases the temperature of the powder bed and local HAZs since the area corresponding to elevated temperatures for a layer, or total HAZ, during its manufacture also increases. During ML-PBF, the powder bed receives more energy in less time and track lengths become shorter due to in-parallel island building; thus, thermal energy has less time to diffuse in between tracks, and local temperatures can increase. This elevated powder bed temperature can prove important

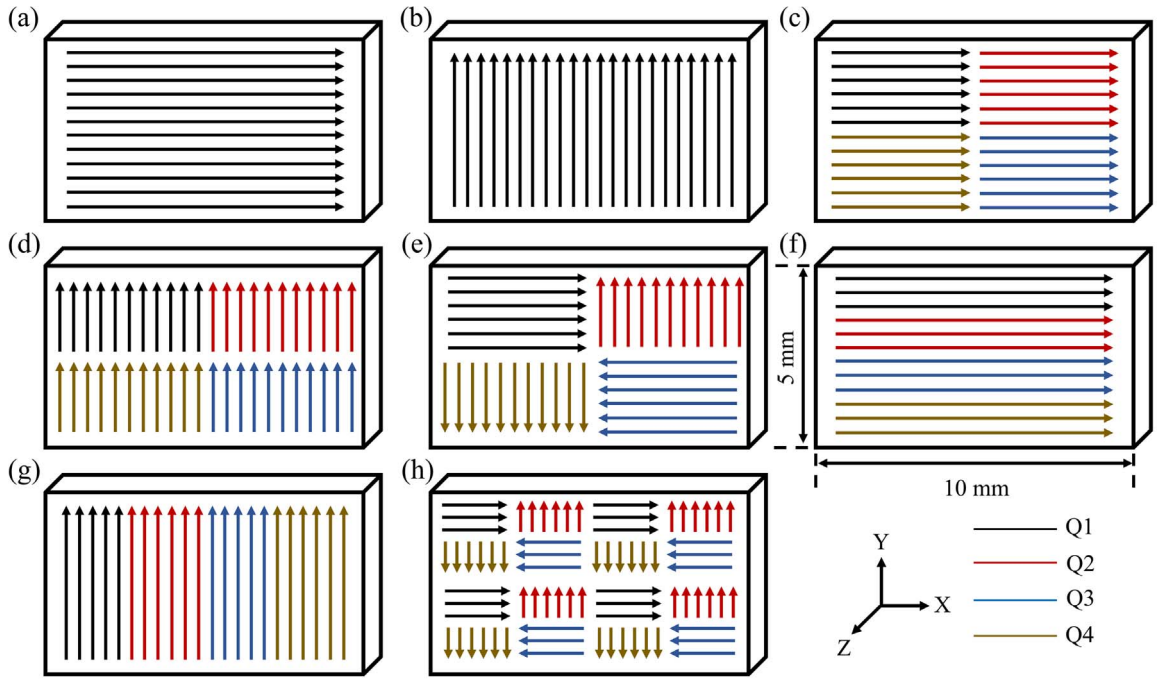

Fig. 5. Schematic of scan patterns used for simulations: (a) SP-A, (b) SP-B, (c) SP-C, (d) SP-D, (e) SP-E, (f) SP-F, (g) SP-G, (h) SP-H; Q1-Q4 refer to sub-islands/islands.

Table 4
Simulations performed for the single- and multi-laser PBF of the 2-layered Ti-6Al-4V parallelepiped.

Sim. #	Scan pattern	# islands (or lasers)	# sub-islands per island	LIP	IDS	Sub-island sequence	Track sweep direction (track scan direction)
S1	SP-A	1	1	0	Full	N/A	Y+ (X+)
S2	SP-C	1	4	1	Quadrant	Q1, Q2, Q3, Q4	Y+ (X+)
S3	SP-C	2	2	3	Halves (X)	(Q1, Q4), (Q2, Q3)	Y+ (X+)
S4	SP-C	4	1	2	Quadrant	N/A	Y+ (X+)
S5	SP-F	4	1	2	Fourths (X)	N/A	Y+ (X+)
S6	SP-B	1	1	0	Full	N/A	X+ (Y+)
S7	SP-D	1	4	1	Quadrant	Q1, Q2, Q3, Q4	X+ (Y+)
S8	SP-D	2	2	3	Halves (Y)	(Q1, Q4), (Q2, Q3)	X+ (Y+)
S9	SP-D	4	1	2	Quadrant	N/A	X+ (Y+)
S10	SP-G	4	1	2	Fourths (Y)	N/A	X+ (Y+)
S11	SP-E	1	4	1	Quadrant	Q1, Q2, Q3, Q4	Y+(X+), X+(Y+), Y-(X-), X-(Y-)
S12	SP-E	4	1	2	Quadrant	N/A	Y+(X+), X+(Y+), Y-(X-), X-(Y-)
S13	SP-H	4	4	3	Quadrant	Q1, Q2, Q3, Q4	Y+(X+), X+(Y+), Y-(X-), X-(Y-)

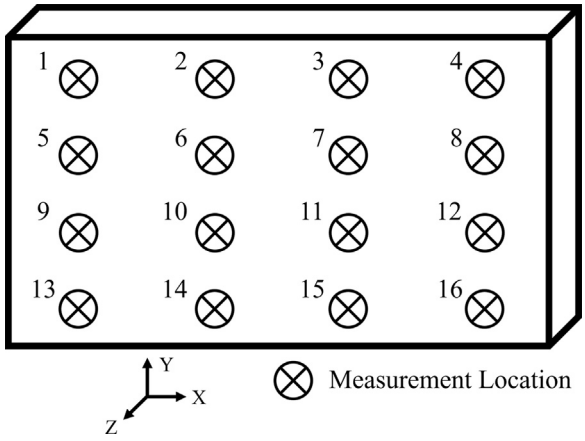

Fig. 6. Schematic of the sixteen measurement locations P1-P16 used to record temperature, temperature gradient and time rate of change.

when calibrating instrumentation to monitor the IR signature of the powder bed. Powder recyclability for use with ML-PBF will most likely be different from that corresponding to single-laser PBF, since surrounding powder bed temperature is slightly more elevated in general; especially for cases in which track lengths are shorter.

For the inspected scan strategies (i.e. S1-S13), material and part geometry, it was found that the number of lasers, and thus the number of HAZs, has little effect on melt pool temperature and morphology during the majority of the build. This is primarily due to the locality of directed laser energy, and the fact that the HAZ is very small relative to the remainder of the powder bed and substrate, which contains a relatively high thermal capacitance. A significant portion of the energy delivered to the powder bed is used for melting and superheating the melt pool; thus, initially hotter powder bed regions do not necessarily translate to hotter melt pools. Initially-hotter powder beds can impact, although slightly, the wetting behavior of the melt pool, local heating rates, HAZ cooling rates, and more; thus ML-PBF of relatively small parts may result in such parts possessing different microstructures than those fabricated using the same process parameters via traditional, single-laser PBF. If the size of the powder bed and/or part were reduced, or if a more convergent scan pattern were employed (i.e. laser relative distances decrease), so that HAZs would be closer to each other more often, then the melt pool shape should be more influenced. The thermal conductivity of the powder bed is very small relative to that of the solidified tracks/part. As a result, the heat transfer through the un-

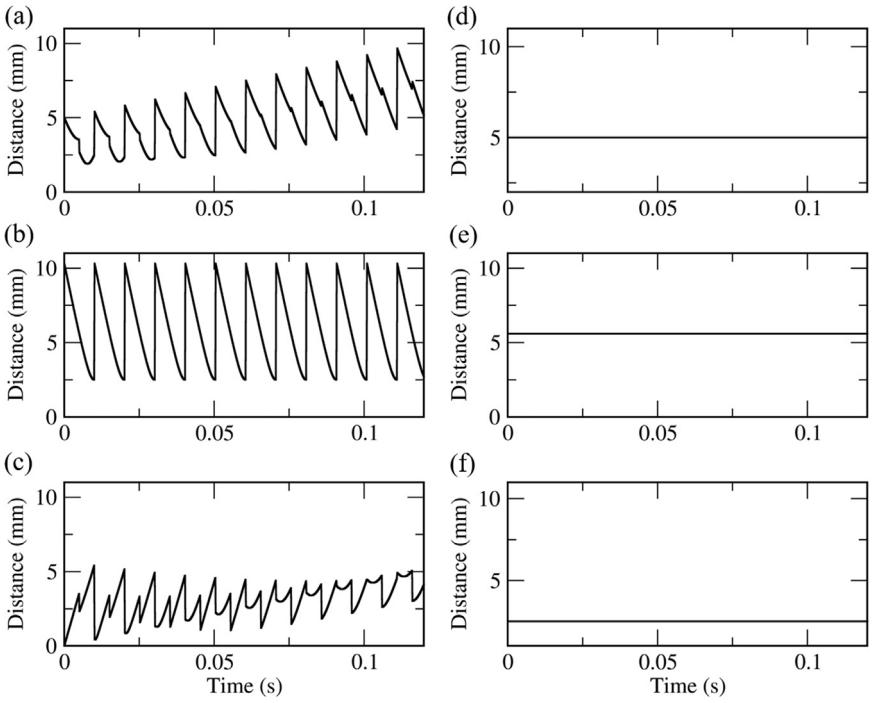

Fig. 7. Relative distance vs. time during S12 between Q1 and (a) Q2, (b) Q3, and (c) Q4; Relative distance vs. time during S4 between Q1 and (d) Q2, (e) Q3, and (f) Q4.

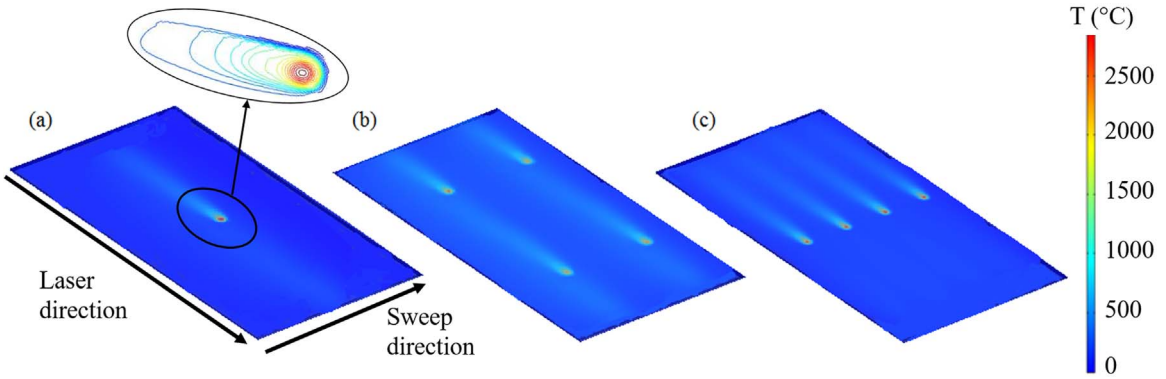

Fig. 8. Temperature response (in °C, with legend shown on right) of powder/part/substrate during L-PBF of first layer for (a) S1, (b) S4 and (c) S5.

melted powder bed is less and melt pool asymmetry exists, as shown in Fig. 8(a). The HAZ temperature is more distributed along the solidified region as opposed to the neighboring powder bed region. All islands receive the same heat flux during processing; thus, only minor differences in peak temperatures, i.e. ± 50 °C, were observed at locations P1-P16 during S1-S13. As expected, the amount of time invested per layer decreases with the addition of each new laser.

The simulated melt pool temperatures were found to possess local extremes around ~2850 °C, located near the center of the penetrating laser beam, as evidenced in Fig. 8. This temperature is significantly higher, by ~1000 °C, than the liquidus temperature of Ti-6Al-4V, indicating a high level of superheat (~50%). Such a superheated melt pool should consist of density and surface tension gradients, and thus free convective and Marangoni-type currents should exist, respectively, within and along the surface of the melt pool. Due to this flow, alloy solutes will be transported and rearranged within a matter of micro-seconds; in addition, contaminants and inert gas may be trapped within the dynamic melt pool. The superheated melt pool is more prone to unstable morphologies, splashing and more [11,62], which can lead to improper fusion and/or pore formation at intermittent locations along a track [63–65]. At these elevated liquid temperatures, amounts of the Ti-6Al-4V alloy powder may vaporize and vapor recoil can occur [62,66]. Note that the predicted peak temperatures should be slightly less due to the melt pool convective transport not being accounted for through use of an accurate effective thermal conductivity. Vapor recoil, natural convection eddies, Marangoni convection and instability, all contribute to the melt pool effective thermal conductivity, and thus, should be considered for more accurate temperature predictions.

Peak temperatures experienced along the first layer of the Ti-6Al-4V parallelepiped during fabrication of its second layer (layer immediately above the first layer) were found to vary between 1700 °C and 1800 °C for all simulations performed. Since the maximum melting temperature of Ti-6Al-4V is ~1660 °C, portions of the first layer will re-melt while the next layer is fabricated. These remelting temperatures will influence fusion behavior of the layer set atop of it, while the solidification behavior of the remelted layer will be influenced by the cooling rates along the new layer. The temperature potential between the new and remelted layer will support residual stress formation upon final fusion. Note that peak temperatures experienced during fabrication of the first and second layers were found to be similar, indicating that melt pool peak temperature may be near independent of layer number for layers near substrate.

The melt pool temperature as predicted from continua-based FEM provides an indirect means to assess conditions conducive for pore

formation, lack of fusion and vaporization. Per use of parameters/conditions reported by Vilaro et al. [61], the simulation results indicate a relatively hot, scan/layer-independent melt pool in excess of 1000 °C its liquidus. These conditions may be conducive for melt pool instability, which can then promote mechanisms for pore formation and lack of fusion. The existence of pores within AM Ti-6Al-4V has proven detrimental to its fatigue behavior, as they serve as stress risers and crack initiation sites [5,67–70]. Any lack of fusion is typically aligned perpendicular to the part build direction (in this case, z), and this introduces a high degree of mechanical anisotropy [4,71]. Hence, control of melt pool temperature may prove beneficial in reducing pore formation; however, the melt pool temperature must remain sufficiently high as to guarantee effective layer-to-layer fusion. Scan planning for ML-PBF should be cognizant of relative distance between melt pools as to ensure that any elevated powder bed temperatures do not drastically affect melt pool wetting behavior, as this can lead to regions of unique microstructure.

4.2. Cooling rates

Local cooling rates are important to quantify, and to design for, as they drive microstructure formation and evolution immediately upon the solidification of the melt pool. To estimate the effect of scan strategy and number of lasers on cooling rates during PBF, an average of all maximum cooling rates extracted at points P1-P16 for each M^{th} layer, i.e. AMCR_M, was determined for all simulations using:

$$\text{AMCR}_M = -\frac{1}{16}\sum_{i=1}^{16}\left(\min\left[\frac{\partial T_i}{\partial t}\right]\right) \tag{29}$$

The uniformity in AMCR, and thus cooling rates, across a layer can influence the homogeneity of the final microstructure of the as-printed part. To quantify this uniformity, a standard deviation of local, maximum cooling rates for a given layer, i.e. the SDCR_M, was found using:

$$\text{SDCR}_M = \sqrt{\sum_{i=1}^{16}\left(-\min\left[\frac{\partial T_i}{\partial t}\right] - \text{AMCR}_M\right)^2/15} \tag{30}$$

The AMCRs and SDCRs corresponding to S1-S13 for the first and second layers are shown graphically in Fig. 9. It may be seen that, in general, $\text{AMCR}_1 > \text{AMCR}_2$, for all scan strategies investigated due primarily to the heat capacitance of the substrate in which the first layer of powder is initially deposited and sintered. The second layer of powder cools off less quickly (by ~80%) since the thermal resistance of the first layer of solidified material decreases the heat transfer rate from the HAZ to the substrate. The AMCR for all simulations investigated is on-the-order of 10^6 °C/s (or ~1 °C/μs). The trends in AMCR were found to be similar for both layers investigated; however, the SDCR trends were not consistent for both layers. Note that although the first layers are typically sacrificial upon completion of PBF, their thermal response are of interest to ensure quality support structures for the non-sacrificial layers of the final part. The maximum cooling rate extracted from each point, P1-P16, along with its AMCR and SDCR, for the first and second layers, are provided in the Appendix A as Tables A1 and A2, respectively.

Fig. 9 indicates that as the number of lasers increases, the AMCR generally decreases, since the amount of energy delivered to the powder bed and part increases regional temperatures (i.e. pre-heat). Higher cooling rates were achievable using the LIP-0, single-laser PBF process with tracks parallel to the part's longest edge and swept in the Y + direction. Lower cooling rates were achieved using the S9, S10 and S13 strategies – which all employed 4 lasers and LIP > 1. As track lengths were reduced via island division and/or sweeping tracks along the longest edge of the part (with tracks parallel to the shortest edge), the cooling rates generally decreased. Introduction of more islands

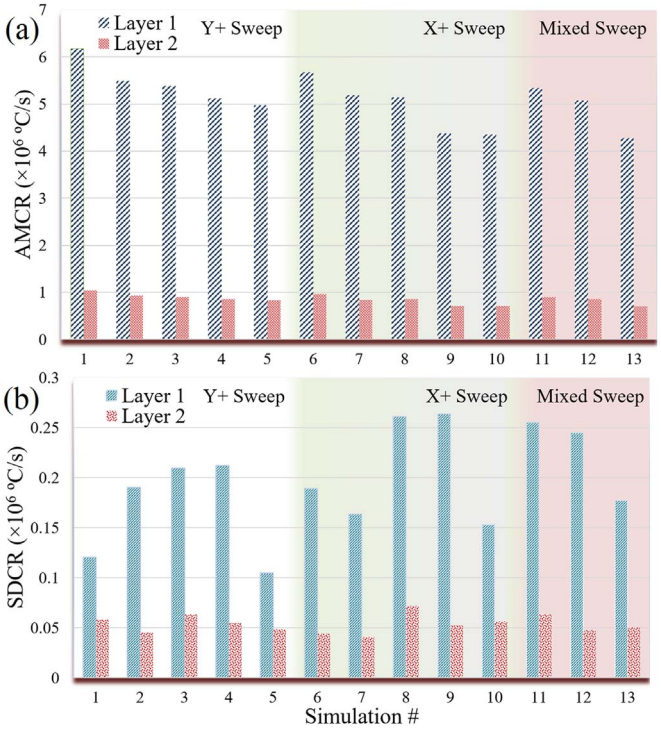

Fig. 9. (a) Average, maximum cooling rate (AMCR) and its (b) standard deviation (SDCR) with respect to first and second layers of Ti-6Al-4V parallelepiped during its manufacture via L-PBF/ML-PBF using scan strategies S1-S13.

and/or lasers generally decreases maximum cooling rates. Comparing S4, S9 and S12, which all employ the quadrant IDS and 4 lasers, but consist of different track sweep directions, i.e. Y+, X+ and mixed, respectively, it is evident that the cooling rate decreases when tracks are swept along the part's longest edge.

The relative distance between melt pools during layer fabrication may not have a significant effect on maximum cooling rates. As shown in Fig. 7, S12 provides for time-varying relative distances between island melt pools, while for S4, the melt pools maintain a constant distance relative to each other; however, in both cases, the AMCRs are similar. Although the AMCR may be more independent of relative melt pool motion (at least for the scan patterns investigated herein), the cooling rates experienced during S12 are less homogeneous over the layer as evidenced by its higher SDCR. Employing a mixed sweeping strategy, in general, will increase the SDCR of a layer. Per Tables A1 and A2, cooling rates are generally highest at the start of a track and decrease along the track length due to heat accumulation effects.

The effect of IDS on layer cooling rates is best evidenced by comparing S4 and S5 with S9 and S10. Although the 'quadrant' and 'fourths' division schemes provide for similar AMCRs, the SDCRs are significantly different. For both the X+ and Y+ track sweeping directions, the fourths IDS can reduce the SDCR by approximately 50% relative to the quadrant IDS. This indicates that more homogeneous microstructures are obtained by employing IDSs consisting of islands aligned successively next to each other, in a single row and with border lines parallel to track scan directions, as opposed to IDSs consisting of islands 'split' by intersecting border lines at the center of the layer. The sweep direction proves important when employing sub-islands for a single laser; meaning, when going from LIP-0 to LIP-1 (e.g. S1 to S2 or S6 to S7), the SDCR can be better controlled when employing islands that have tracks swept parallel to the part's longest edge. Layers fabricated using a single laser and a single sub-island, with tracks parallel to the longest edge, proved to have the highest cooling rates while also having a relatively low SDCR. Increasing the number of lasers, as evidenced by comparing S2-S4 (or S7-S9), in which each of

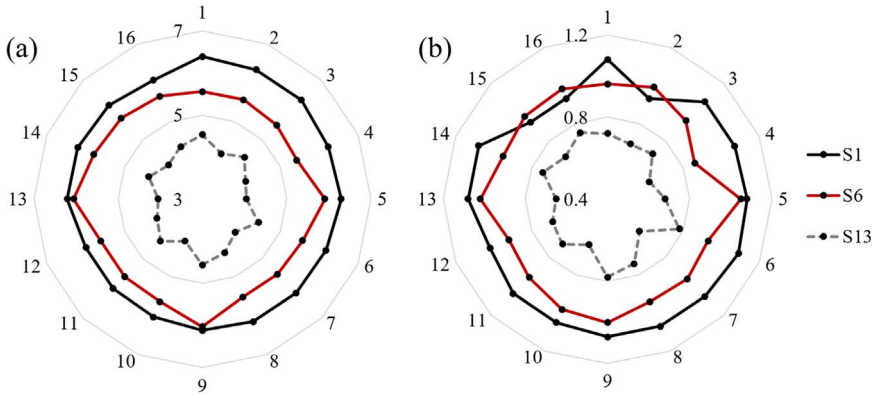

Fig. 10. Radar charts showing maximum cooling rates (in units 10^6 °C/s) measured at points P1-P16 (circumferential markings) during manufacture of the Ti-6Al-4V parallelepiped following scan strategies described in S1, S6 and S13 (star/circular profiles) for the (a) first layer and (b) second layer.

these simulations employ either 1, 2 or 4 lasers, respectively, will decrease AMCR, but the decrease going from 2 to 4 lasers is significantly less drastic.

Fig. 10 shows the maximum cooling rates measured at P1-P16 along the first two layers of the Ti-6Al-4V parallelepiped for S1, S6 and S13 in the form of radar charts. These radar charts provide a unique means for visualizing homogeneity in maximum cooling rates with respect to each layer; assuming the discrete 'measuring points', i.e. like P1-P16, are arranged in an appropriate manner. For example, using the P1-P16 scheme provided in Fig. 6, generated radar charts appear more circular in shape when the maximum cooling rate varies less with location along the layer for a given scan pattern; while they appear more 'star-shaped' with increased inhomogeneity. For all simulations, the maximum cooling rate varies with location along the layer (i.e. no perfect circle exists). In general, homogeneity in maximum cooling rates is higher for the first layer relative to the second layer, and this can be attributed to the thermal capacitance of the substrate. Increasing the LIP order will dissolve a 'perfect circle', i.e. similar to S1, to a more staggered shape since more variation and fluctuation in cooling rate will exist due to more lasers and sub-islands. Low LIP scan patterns allow each layer to possess a thermal response less influenced by other lasers.

Based on the results herein, Ti-6Al-4V will cool very rapidly from temperatures well above its β-transus (~995 °C) during L-PBF. Microstructural phase transformations are then highly influenced by the magnitude and time-rate-of-change of local cooling rates. Many have verified the dominance of the martensite phase in PBF Ti-6Al-4V [43,72–75], and this can be attributed to the very fast cooling rates encountered upon solidification of the melt pool, as confirmed herein as ~10^5–10^6 °C/s. Maintaining these high cooling rates during PBF will preserve the amount of martensite in the final Ti-6Al-4V material. Elevated powder bed temperatures can promote α' martensite decomposition, while sustained temperature gradients can lead to a complete α+β phase. [73]. Although the current work has focused on maximum cooling rates, the sustained cooling rates inherent to ML-PBF should be lower relative to single-laser PBF due to the more elevated powder bed temperatures. Thus, increasing the number of lasers for PBF may promote more martensite decomposition and a final Ti-6Al-4V material with less martensite. The various scan patterns will influence the elongated grain growth directions within the Ti-6Al-4V material. As shown by Thijs [72], the elongated grains will follow the direction of the conductive heat flux. Thus, layers fabricated using scan patterns that provide for relatively high SDCRs and time-variant relative motion of melt pools, i.e. S11-S13, will possess more anisotropic microstructure.

4.3. Temperature gradients

In general, parts made via L-PBF experience very high temperature gradients, and such gradients can drive residual stress formation [15,73,76]. The rapid, localized heating/cooling of the melt pool during L-PBF promotes material expansion and contraction at non-equal rates, thus forming micro- and macro-stresses within the solid part volume. In addition, these thermal stresses can lead to the occurrence of segregation phenomena and the presence of non-equilibrium phases [72]. Residual stress can prove detrimental to the fatigue behavior of Ti-6Al-4V during its application [5,77]. The temperature-dependent properties of Ti-6Al-4V are somewhat supportive to residual stress formation during PBF [22]. Relative to many other common AM metals, Ti-6Al-4V has a low thermal diffusivity, resulting in more thermal energy build-up as opposed to its transport, and thus, over the same time window, Ti-6Al-4V will have higher local temperature gradients.

Herein, local temperature gradient magnitudes are extracted and used for predicting the existence of thermal stress, which can lead to, most often, tensile residual stress in the part [18]. An average maximum temperature gradient magnitude from points P1-P16 corresponding to the M^{th} layer, i.e. AMTG_M, was determined for S1-S13 using:

$$\text{AMTG}_M = \frac{1}{16}\sum_{i=1}^{16}\left(\max\|\nabla T_i\|\right) \tag{31}$$

In addition, the homogeneity of AMTGs along a layer was quantified by taking their standard deviation, i.e. the SDTG_M:

$$\text{SDTG}_M = \sqrt{\sum_{i=1}^{16}\left(\max\|\nabla T_i\| - \text{AMTG}_M\right)^2 \Big/ 15} \tag{32}$$

The AMTGs and SDTGs for each layer during S1-S13 are shown in Fig. 11. Similar to trends observed for cooling rates, the AMTGs and SDTGs are generally lower during fabrication of the second layer which has less heat transfer to the substrate. The AMTG is high, on-the-order of 20–100 °C/μm for all simulations. In addition, the AMTG varies along the layer; being higher at points near the start of a track and lower toward the end of a track, primarily due to heat accumulation effects [36]. The magnitude of the temperature gradient also decreases with laser sweep direction; meaning, as the part grows in volume, and the surrounding media accumulates more heat, later tracks will experience lower AMTGs. This confirms that regional preheat can reduce residual stress formation, as local temperature gradients become less severe during final track fabrication. All maximum temperature gradient magnitudes at P1-P16 during fabrication of the first layer and second layer are summarized in Tables A3 and A4, respectively.

By comparing AMTGs in Fig. 11(a), it may be concluded that employing more lasers via ML-PBF can reduce the magnitudes of temperature gradients by ~5%. A ~10% reduction in AMTG is achieved

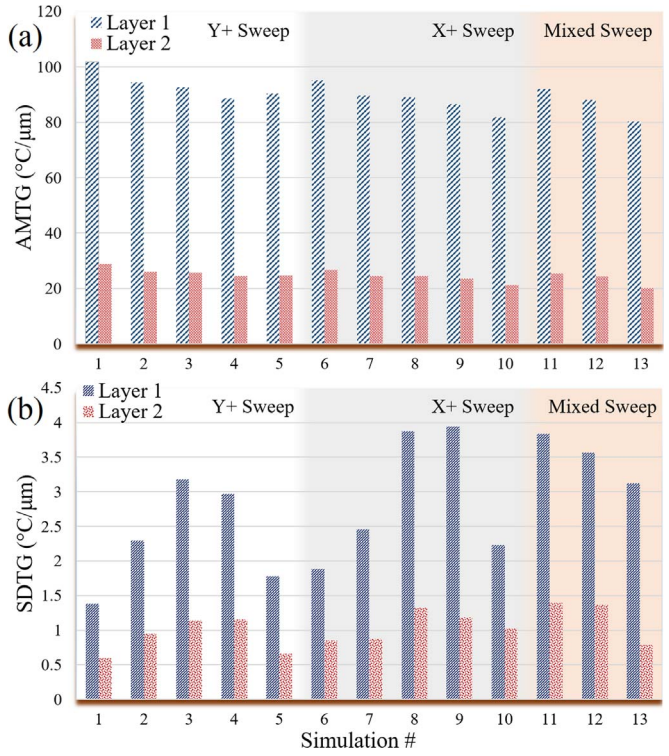

Fig. 11. (a) Average, maximum temperature gradient magnitude (AMTG) and its (b) standard deviation (SDTG) with respect to first and second layers of Ti-6Al-4V parallelepiped during its manufacture via L-PBF/ML-PBF using scan strategies S1-S13.

by employing the 'fourths' IDS instead of the 'quadrant' IDS, indicating the importance of island geometries relative to layer geometry. Building layers in a sequenced island approach, i.e. LIP-1/LIP-3 decreases the AMTG (i.e. S1 vs. S2, S6 vs. S7 and S12 vs. S13) for both layers. Lower AMTGs exist when sweeping lasers in the X-direction, along the longest dimension of the parallelepiped, with tracks parallel to the shortest edge. By comparing the results from S1 and S6 in Fig. 11, scan patterns with smaller tracks (S6) result in lower temperature gradients as compared to patterns with longer tracks (S1). This is due to the time interval between the fusion of neighboring points on an island with shorter tracks being smaller than that for islands with longer tracks. Longer time intervals allow heat to diffuse, while shorter time intervals result in more retained heat and thus higher temperature. The synchronous, mixed-sweeping technique investigated (i.e. P=4) demonstrates to provide for the lowest AMTG. Li et al. [18] demonstrated similar results for single-laser, mixed-direction/island scanning.

The SDTG provides insight into the spatial uniformity of AMTG and a means for characterizing the complexity of a residual stress distribution. Fig. 11(b) provides the SDTGs for S1-S13, while Fig. 12 provides radar charts of the AMTGs. Since the scan strategy related to S1 was found to provide the lowest SDTG, its radar chart possesses a more circular shape, while S13, has a more staggered profile due to its higher SDTG. In general, strategies providing for lower AMTGs tend to have higher SDTGs. For example, S1, S6 and S13 provide for the highest AMTG for their respective sweep strategy, while in contrast, these same strategies possess the lowest SDTG in their category. Lower SDTGs, unlike the AMTG, were found to exist when sweeping lasers in the Y-direction, along the shortest dimension of the parallelepiped, with tracks parallel to the longest edge. Mixed-sweeping techniques demonstrated to provide the highest SDTG when using one or four lasers.

Results suggest that increasing the total number of sub-islands (e.g. S1 to S2 to S13) will decrease the AMTG and increase the SDTG of a layer. Utilizing an IDS cognizant of the part shortest edge can provide a significant reduction in SDTG. For example, the 'fourths' IDS appears to be more appropriate for the multi-laser approach, since its SDTG is comparable to that experienced for a unit-island layer (LIP-0). The mixed sweep approach for accomplishing single- (i.e. S11) or multi-laser PBF (i.e. S12 and S13) provides less homogeneity in AMTGs; however, the lowest overall AMTG was accomplished using S13. The mixed-sweep strategy (i.e. SP-E, SP-H), in contrast to both the X and Y scan strategies (i.e. SP-A through SP-D), possesses an SDTG that decreases as more islands and lasers are introduced.

Scan strategies consisting of melt pools with time-variant relative distances can lead to higher STDGs. Fig. 13 presents the response of local temperature and its gradient as a Q1 laser (see Fig. 5) passes a point centered on its respective island, for S1, S4 and S9. Note that the time to complete the presented islands ranges from 100 ms (for S1 and S4) to 400 ms (for S9). From Fig. 13(a)–(c), it may be seen that the peak temperatures experienced are similar. There are slight temperature perturbations before and after local temperature spikes due to the passing of the laser as it scans neighboring, adjacent tracks. These temperature perturbations do not exceed the liquidus temperature of Ti-6Al-4V, so the center region of the track does not remelt. The first temperature perturbation is lower in magnitude than that of the second perturbation due to regional heat accumulation effects. The first temperature perturbation is more pronounced for the S9 strategy (4 lasers, X+ sweeping, quadrant IDS) due to the shorter track lengths providing for a lower track-to-track time interval and more regional preheating. The cooling rates immediately after the laser passes the point-of-interest are much higher than those experienced after the second temperature perturbation. After the adjacent track is finished, the point-of-interest experiences a semi-continuous cooling rate on-the-order of 1000 °C/s for the remainder of the layer building process. This indicates that conditions are highly favorable for martensite

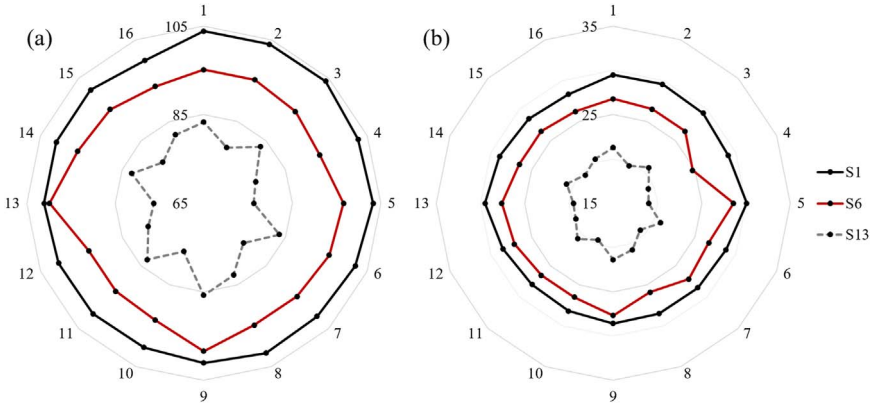

Fig. 12. Radar charts showing maximum temperature gradient magnitudes (in units °C/μm) measured at points P1-P16 (circumferential markings) during manufacture of the Ti-6Al-4V parallelepiped following scan strategies described in S1, S6 and S13 (star/circular profiles) for the (a) first layer and (b) second layer.

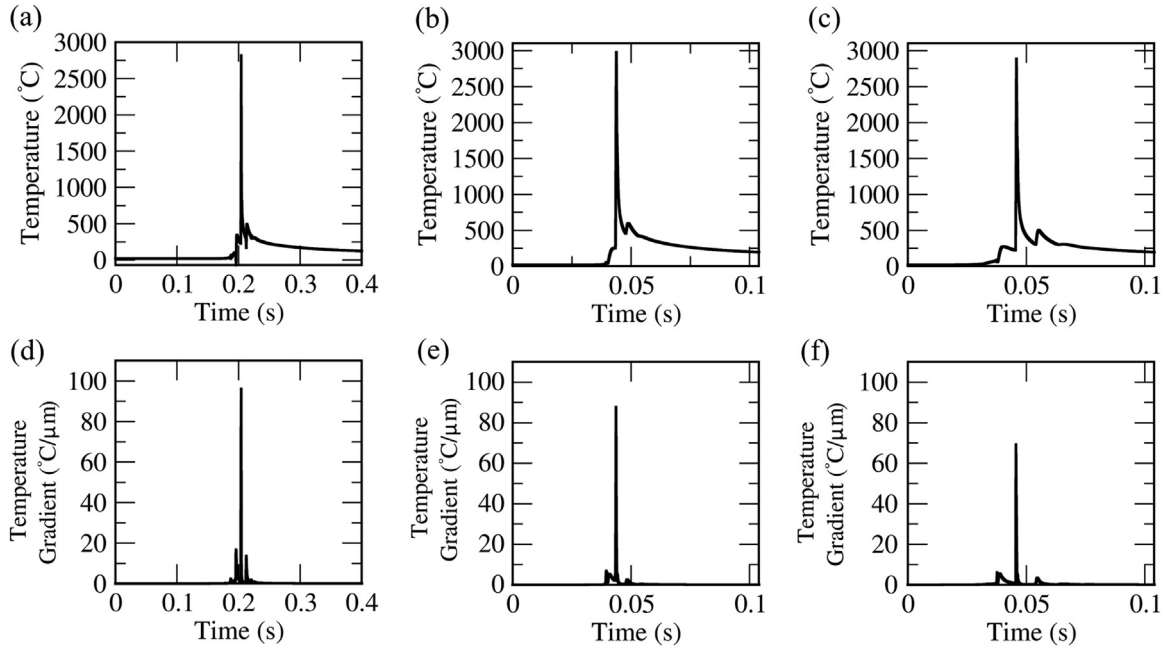

Fig. 13. Temperature response for (a) S1, (b) S4, and (c) S9, as well as the temperature gradient magnitude response for (d) S1, (e) S4, and (f) S9, as the Q1 laser passes its island center.

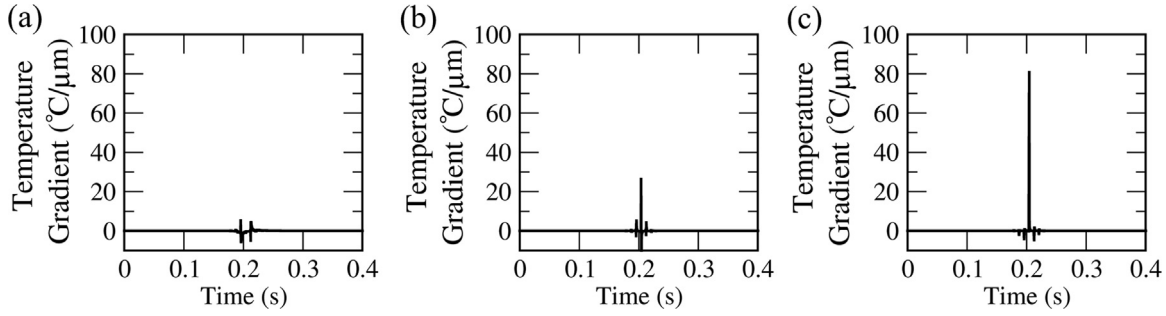

Fig. 14. Response of local temperature gradient as Q1 laser passes center of island during S1: (a) X-component, (b) Y-component, and (c) Z-component.

retention within Ti-6Al-4V parts fabricated by single- or multi-laser PBF.

As shown in Fig. 13(d) – (f), the local temperature gradient magnitude, at the center of the Q1 island for the S1, S4 and S9 scan strategies, also varies with time, LIP and scan direction (i.e. track lengths). The local temperature gradient magnitude at the point-of-interest achieves maximums on-the-order of 60–90 °C/μm, with the lowest peak occurring for S9 – the simulation employing 4 lasers (LIP-2) and shorter tracks parallel to the part's shortest edge. These high, instantaneous temperature gradients support the formation of tensile residual stress in the center of the island; however, the scanning of tracks immediately atop the point-of-interest may elevate its temperature to liquidus, thus 'erasing' any encumbered residual stress. The instantaneous temperature gradients experienced by the point-of-interest during the PBF of the layer directly above it will be less in magnitude, by ~30%, due to less heat penetration. Hence, the free surface of the final parts should consist of higher residual stress. The difference between peak temperatures of adjacent layers (of thickness =30 μm) was found to be ~1000 °C for many of the scan strategies investigated, and this confirms a layer-wise temperature gradient (Z direction) around 30 °C/μm. There are perturbations in temperature gradient magnitude when the laser scans the neighboring tracks. Since the track scanned before the point-of-interest's track provides for a bigger temperature difference, as less preheat is available, the first perturbation is higher in magnitude. Note that the highest temperature gradient magnitude was measured to occur for S1 (LIP-0) which consisted of a single laser, a single island, and long tracks parallel to the part's longest edge. Increasing the laser number to 4, i.e. S1 to S4, results in a local decrease in temperature gradient magnitude by ~10%. Based on Fig. 13(d)- (f), it appears that local residual stress formation is more sensitive to track scan directions and not number of lasers employed, as evidenced by comparing the percent decrease between S1 and S4, and the S1 and S9.

The local temperature gradient will depend on the scan direction of the employed laser(s). As shown in Fig. 14, the temperature gradient inherent to the point-of-interest during S1 has a high Z-component and a low X- and Y-component. It was consistently found that the temperature gradient parallel to the laser scan direction is the lowest, and this agrees with the results of Mercelis et al. [15] and Li et al. [18]. Unidirectional, single-island scanning similar to S1 will have more points along the layer experience a similar thermal history, and thus, its SDTG will be low and the residual stress along the X and Y directions will be more uniform, and this agrees with the results presented by Li et al. [18], as well.

5. Conclusions

A continuum-based, numerical model was developed for simulating the heat transfer during single-laser powder bed fusion (L-PBF) and multi-laser powder bed fusion (ML-PBF) of Ti-6Al-4V for elucidating process-property relationships while varying number of lasers and scan strategy employed. Effects of various synchronous, orthogonal scan patterns, island division schemes (IDSs) and levels of island planning (LIP) on the temperature response during the fusion of the first and

second layers of a multi-track Ti-6Al-V parallelepiped were investigated. The major findings discovered from the conducted simulations, as they pertain to the inspected scan strategies, material and part geometry, are summarized below:

1) The use of more lasers during PBF significantly decreases production times as the build rate per layer increases. As the number of lasers increases, the average powder bed temperature and total HAZ area increases, thus reducing local temperature gradients and cooling rates.
2) Peak melt pool temperatures were found to be near-independent of the scan strategy and number of lasers used per layer. Melt pools were predicted to have peak temperatures around 2500 °C; neighboring points within the layer immediately below were found to have temperatures just above liquidus for effective remelting and fusion.
3) Peak cooling rates were found to be on the order of 10^6 °C/s, and semi-continuous cooling rates were found to be on-the-order of 10^3 °C/s during the L-PBF process investigated. These rates are conducive for martensitic microstructure formation in Ti-6Al-4V. Microstructural anisotropy will be higher in parts fabricated via island-based ML-PBF.
4) Maximum temperature gradient magnitudes were found to be on-the-order of 50 °C/μm. Local temperature gradients were confirmed to be direction-dependent and to consist of low track/scan-wise (X) and sweep-wise (Y) components and significantly higher layer/height-wise (Z) components.
5) The IDS, and thus track length with respect to a part's shortest edge, both have a significant influence on a layer's temperature response, cooling rate and temperature gradients. Employing IDSs that provide for a unit-row of islands sequenced along the longest edge of a part allows for shorter track lengths and reduced residual stress magnitudes. Using multi-laser scan strategies that provide for time-variant relative position between lasers will result in a more complex, anisotropic residual stress distribution along the layer of a part.
6) The LIP dictates the number of lasers employed and whether or not sub-islands exist for a given layer; LIP-0 corresponds to single-island/single-laser approaches, LIP-1 corresponds to multi-island/single-laser approaches, LIP-2 corresponds to single-pass ML-PBF (i.e. one island per laser) and LIP-3 corresponds to multi-island ML-PBF. The results indicate that the LIP will affect temperature gradients and cooling rates.

The ongoing standardization efforts focused on 'scaling' AM process parameters from building microstructurally-similar, certifiable specimens to application-worthy components depends on effectively predicting the thermomechanical response of parts with various geometry and size. Size and time interval effects, as shown by the simulations herein, result in different residual stress and microstructure distributions. A thermal 'transfer function' is needed to go from specimen scale to component scale, and simulations of the PBF process for characterizing new machine improvements, such as ML-PBF, as well learning process-property-performance relationships will continue to be needed moving forward. These 'transfer functions' can allow for determining how process parameters should be scaled for achieving components of the same microstructural properties and defect statistics as those of lab-scale, testing specimens.

Acknowledgement

This work was supported by the National Science Foundation under Grant #1657195.

Appendix A

See Tables A1–A4.

Table A1
Maximum cooling rates (with average and standard deviation) at locations P1-P16 following scan patterns described per S1-S13 during fabrication of first layer; units in 10^6 °C/s.

	S1	S2	S3	S4	S5	S6	S7	S8	S9	S10	S11	S12	S13
Point 1	6.39	5.94	5.91	5.49	5.13	5.55	5.28	5.31	4.53	4.26	5.91	5.52	4.53
Point 2	6.33	5.61	5.46	5.01	5.01	5.55	4.98	4.83	4.05	4.23	5.61	4.89	4.17
Point 3	6.33	5.55	5.61	5.31	4.95	5.49	5.22	5.31	4.44	4.14	5.13	4.98	4.41
Point 4	6.24	5.46	5.52	5.19	4.77	5.43	5.01	4.98	4.11	4.08	4.95	4.74	4.11
Point 5	6.30	5.49	5.43	5.13	5.07	5.91	5.43	5.46	4.77	4.35	5.49	5.16	4.05
Point 6	6.18	5.31	5.13	4.92	5.07	5.58	5.22	5.13	4.29	4.29	5.31	4.71	4.44
Point 7	6.15	5.46	5.31	5.04	4.92	5.52	5.34	5.49	4.59	4.26	5.25	5.13	4.11
Point 8	6.15	5.25	5.19	4.95	4.83	5.52	5.16	5.13	4.59	4.17	5.19	5.07	4.38
Point 9	6.12	5.73	5.52	5.52	5.07	6.03	5.13	4.89	4.59	4.44	5.61	5.31	4.56
Point 10	6.03	5.61	5.37	4.83	4.89	5.64	5.01	4.71	3.96	4.53	5.52	5.61	4.08
Point 11	6.00	5.61	5.49	5.40	4.83	5.61	5.28	4.92	4.29	4.35	5.19	5.13	4.41
Point 12	6.00	5.49	5.31	5.13	4.89	5.61	4.89	4.86	3.93	4.38	4.98	5.01	4.17
Point 13	6.21	5.52	5.31	5.01	5.01	6.06	5.40	5.43	4.68	4.59	5.49	4.89	4.05
Point 14	6.21	5.28	5.19	4.89	5.07	5.79	5.13	5.28	4.53	4.53	5.31	5.13	4.38
Point 15	6.15	5.4	5.37	5.07	4.98	5.73	5.37	5.49	4.41	4.5	5.28	4.98	4.14
Point 16	6.06	5.19	5.04	4.98	5.01	5.64	5.04	5.01	4.17	4.47	5.13	4.98	4.35
Average	6.18	5.49	5.38	5.12	4.97	5.67	5.18	5.14	4.37	4.35	5.33	5.08	4.27
Standard deviation	0.12	0.19	0.21	0.21	0.11	0.19	0.16	0.26	0.26	0.15	0.26	0.25	0.18

Table A2
Maximum cooling rates (with average and standard deviation) at locations P1-P16 following scan patterns described per S1-S13 during fabrication of second layer; units in 10^6 °C/s.

	S1	S2	S3	S4	S5	S6	S7	S8	S9	S10	S11	S12	S13
Point 1	1.08	1.05	1.05	0.94	0.87	0.96	0.88	0.89	0.75	0.66	1.08	0.93	0.72
Point 2	0.93	0.95	0.91	0.85	0.86	0.99	0.71	0.89	0.65	0.65	0.96	0.85	0.69
Point 3	1.07	0.93	0.94	0.86	0.82	0.94	0.84	0.89	0.71	0.65	0.84	0.86	0.71
Point 4	1.07	0.92	0.95	0.93	0.89	0.86	0.85	0.86	0.69	0.61	0.85	0.77	0.62
Point 5	1.08	0.94	0.86	0.86	0.84	1.05	0.86	0.99	0.74	0.78	0.94	0.81	0.68
Point 6	1.09	0.89	0.85	0.86	0.84	0.93	0.84	0.84	0.67	0.66	0.89	0.77	0.78
Point 7	1.07	0.97	0.86	0.86	0.82	0.95	0.87	0.94	0.79	0.66	0.85	0.84	0.62
Point 8	1.07	0.86	0.93	0.77	0.71	0.94	0.89	0.84	0.75	0.65	0.88	0.84	0.74
Point 9	1.07	0.99	0.95	0.95	0.84	1.00	0.85	0.71	0.79	0.71	0.91	0.89	0.78
Point 10	1.05	0.93	0.81	0.74	0.82	0.98	0.85	0.71	0.64	0.75	0.91	0.95	0.64
Point 11	1.05	0.91	0.94	0.85	0.74	0.94	0.82	0.89	0.69	0.71	0.88	0.85	0.71
Point 12	1.02	0.94	0.86	0.85	0.86	0.92	0.82	0.85	0.63	0.77	0.86	0.83	0.69
Point 13	1.08	0.93	0.86	0.85	0.85	1.02	0.85	0.10	0.71	0.75	0.94	0.85	0.65
Point 14	1.08	0.89	0.93	0.82	0.86	0.95	0.85	0.82	0.75	0.75	0.89	0.84	0.74
Point 15	0.93	0.91	0.81	0.84	0.89	0.97	0.81	0.85	0.75	0.75	0.82	0.86	0.69
Point 16	0.93	0.89	0.86	0.89	0.86	0.98	0.86	0.83	0.65	0.78	0.85	0.86	0.75
Average	1.04	0.93	0.90	0.86	0.83	0.96	0.84	0.81	0.71	0.70	0.90	0.85	0.70
Standard deviation	0.06	0.05	0.06	0.06	0.05	0.04	0.04	0.20	0.05	0.06	0.06	0.05	0.05

Table A3
Maximum temperature gradient magnitudes (with average and standard deviation) at locations P1-P16 following scan patterns described per S1-S13 during fabrication of first layer; units in °C/μm.

	S1	S2	S3	S4	S5	S6	S7	S8	S9	S10	S11	S12	S13
Point 1	103.9	98.1	100.5	94.3	93.4	95.2	91.2	90.5	88.5	83.4	100.6	93.8	83.3
Point 2	103.9	96.5	93.9	87.1	91.2	95.2	86.7	84.5	81.7	79.9	96.2	85.3	78.6
Point 3	104.0	95.2	95.5	91.6	90.3	94.3	90.3	91.5	87.6	78.6	88.5	86.7	83.1
Point 4	102.8	93.9	94.8	89.8	87.1	93.4	87.2	86.7	82.6	77.7	86.5	83.1	77.7
Point 5	103.3	95.3	93.5	88.9	92.1	96.6	93.5	93.9	92.5	81.7	94.5	89.4	76.3
Point 6	102.1	92.5	88.5	85.8	91.1	95.7	90.3	88.5	85.3	80.8	91.5	82.6	83.5
Point 7	101.2	94.9	90.5	87.6	89.8	94.8	92.1	94.5	89.8	80.4	90.7	88.9	77.7
Point 8	101.7	91.5	89.9	86.2	88.5	94.8	89.4	88.5	89.8	79.5	89.8	88.0	82.6
Point 9	101.1	97.0	94.8	94.8	92.5	98.5	88.5	85.5	89.8	83.1	96.1	91.6	85.8
Point 10	100.3	95.5	92.5	85.5	89.8	93.6	87.1	82.6	80.4	84.4	94.8	96.1	76.8
Point 11	100.4	96.1	94.5	91.2	88.0	93.2	91.2	85.8	85.3	81.7	89.8	88.9	83.1
Point 12	100.5	94.5	92.0	88.9	88.9	93.2	85.5	84.9	79.9	82.2	86.7	87.1	78.6
Point 13	101.1	94.8	91.5	87.1	91.6	99.9	93.0	93.4	91.2	85.3	94.5	85.3	76.3
Point 14	101.1	91.2	89.8	85.3	92.1	95.9	88.9	91.2	88.9	84.4	91.5	88.9	82.6
Point 15	101.2	93.0	91.5	88.0	90.7	95.0	92.5	94.3	87.1	83.3	91.2	86.7	78.1
Point 16	99.9	89.5	87.6	86.7	88.9	93.6	87.6	87.1	83.5	83.5	88.9	86.7	81.7
Average	101.8	94.3	92.6	88.7	90.4	95.2	89.7	88.9	86.5	81.9	92.0	88.1	80.4
Standard deviation	1.38	2.29	3.17	2.97	1.78	1.88	2.45	3.87	3.94	2.22	3.84	3.56	3.12

Table A4
Maximum temperature gradient magnitudes (with average and standard deviation) at locations P1-P16 following scan patterns described per S1-S13 during fabrication of second layer; units in °C/μm.

	S1	S2	S3	S4	S5	S6	S7	S8	S9	S10	S11	S12	S13
Point 1	29.5	28.3	28.0	26.5	24.7	26.8	24.4	25.6	24.3	20.1	28.6	27.1	21.3
Point 2	29.6	26.5	26.1	23.8	24.4	26.5	22.8	23.5	22.0	20.5	26.5	23.5	19.6
Point 3	29.4	26.5	26.5	25.0	24.9	26.5	24.7	25.0	23.2	21.0	25.0	23.7	20.7
Point 4	29.1	26.1	27.1	25.2	23.5	24.7	23.5	23.7	22.0	19.9	23.5	22.6	19.3
Point 5	30.1	25.8	25.6	25.3	25.5	28.6	25.0	26.1	25.2	21.0	26.5	25.3	19.0
Point 6	28.8	25.0	25.0	24.1	25.2	26.7	24.9	25.5	23.5	20.8	25.0	22.0	20.8
Point 7	28.5	26.1	25.5	23.2	25.0	27.1	25.5	26.5	25.0	20.1	25.0	24.3	19.3
Point 8	28.5	25.5	25.0	23.5	24.1	25.9	25.3	25.5	24.6	20.5	25.0	23.8	20.7
Point 9	28.6	26.8	27.1	27.1	25.3	27.7	25.0	23.5	25.3	21.4	26.5	25.0	21.4
Point 10	28.2	26.5	25.0	23.4	25.0	26.5	23.5	22.0	22.4	22.4	27.1	26.4	19.5
Point 11	28.0	25.8	26.5	25.0	23.5	26.5	24.4	24.1	23.6	20.3	25.0	25.4	20.7
Point 12	28.5	26.5	25.6	25.0	24.3	27.1	23.5	23.1	21.7	21.1	22.8	23.8	19.6
Point 13	29.5	27.1	25.0	23.6	25.0	27.6	25.5	25.2	24.4	22.9	25.9	23.5	19.5
Point 14	28.9	24.3	25.0	23.7	25.5	26.5	25.0	24.4	24.3	22.7	25.5	25.8	20.7
Point 15	28.5	25.5	25.5	23.6	24.9	26.5	25.0	26.5	23.5	21.7	24.4	23.7	19.5
Point 16	28.3	25.0	23.2	23.7	25.7	26.2	23.2	23.5	22.8	22.9	25.5	23.7	20.4
Average	28.9	26.1	25.7	24.5	24.8	26.7	24.4	24.6	23.6	21.2	25.5	24.4	20.1
Standard deviation	0.59	0.95	1.14	1.16	0.66	0.85	0.87	1.33	1.18	1.03	1.39	1.37	0.78

References

[1] X. Wang, S. Xu, S. Zhou, W. Xu, M. Leary, P. Choong, M. Qian, M. Brandt, Y.M. Xie, Topological design and additive manufacturing of porous metals for bone scaffolds and orthopaedic implants: a review, Biomaterials 83 (2016) 127–141. http://dx.doi.org/10.1016/j.biomaterials.2016.01.012.

[2] W.E. Frazier, Metal additive manufacturing: a review, J. Mater. Eng. Perform. 23 (2014) 1917–1928. http://dx.doi.org/10.1007/s11665-014-0958-z.

[3] S.M. Thompson, L. Bian, N. Shamsaei, A. Yadollahi, An overview of Direct Laser Deposition for additive manufacturing; Part I: transport phenomena, modeling and diagnostics, Addit. Manuf. 8 (2015) 36–62. http://dx.doi.org/10.1016/j.addma.2015.07.001.

[4] N. Shamsaei, A. Yadollahi, L. Bian, S.M. Thompson, An overview of Direct Laser Deposition for additive manufacturing; Part II: mechanical behavior, process parameter optimization and control, Addit. Manuf. 8 (2015) 12–35. http://dx.doi.org/10.1016/j.addma.2015.07.002.

[5] A. Yadollahi, N. Shamsaei, Additive Manufacturing of Fatigue Resistant Materials: challenges and Opportunities, Int. J. Fatigue 98 (2017) 14–31. http://dx.doi.org/10.1016/j.ijfatigue.2017.01.001.

[6] C.R. Deckard, Method and apparatus for producing parts by selective sintering Patent #: US 4863538 A,1989.

[7] M. Masoomi, N. Shamsaei, X. Gao, S.M. Thompson, A. Elwany, L. Bian, N. Shamsaei, L. Bian, A. Elwany, Modeling, simulation and experimental validation of heat transfer during selective laser melting, in: ASME 2015 International Mech. Eng. Congr. Expo., ASME, Houston, Texas, USA, 2015: p. V02AT02A007. doi:http://dx.doi.org/10.1115/IMECE2015-52165.

[8] E.R. Denlinger, V. Jagdale, G. Srinivasan, T. El-Wardany, P. Michaleris, Thermal modeling of Inconel 718 processed with powder bed fusion and experimental validation using in situ measurements, Addit. Manuf. 11 (2016) 7–15. http://dx.doi.org/10.1016/j.addma.2016.03.003.

[9] F. Verhaeghe, T. Craeghs, J. Heulens, L. Pandelaers, A pragmatic model for selective laser melting with evaporation, Acta Mater. 57 (2009) 6006–6012. http://dx.doi.org/10.1016/j.actamat.2009.08.027.

[10] R.S. Khmyrov, S.N. Grigoriev, A.A. Okunkova, A.V. Gusarov, On the possibility of selective laser melting of quartz glass, Phys. Procedia 56 (2014) 345–356. http://dx.doi.org/10.1016/j.phpro.2014.08.117.

[11] S.A. Khairallah, A.T. Anderson, A. Rubenchik, W.E. King, Laser powder-bed fusion additive manufacturing: physics of complex melt flow and formation mechanisms of pores, spatter, and denudation zones, Acta Mater. 108 (2016) 36–45. http://dx.doi.org/10.1016/j.actamat.2016.02.014.

[12] D. Gu, P. Yuan, Thermal evolution behavior and fluid dynamics during laser additive manufacturing of Al-based nanocomposites: underlying role of reinforcement weight fraction, J. Appl. Phys. 118 (2015) 233109. http://dx.doi.org/10.1063/1.4937905.

[13] C. Weingarten, D. Buchbinder, N. Pirch, W. Meiners, K. Wissenbach, R. Poprawe, Formation and reduction of hydrogen porosity during selective laser melting of AlSi10Mg, J. Mater. Process. Technol. 221 (2015) 112–120. http://dx.doi.org/10.1016/j.jmatprotec.2015.02.013.

[14] A.M. Khorasani, I. Gibson, M. Goldberg, G. Littlefair, A survey on mechanisms and critical parameters on solidification of selective laser melting during fabrication of Ti-6Al-4V prosthetic acetabular cup, Mater. Des. 103 (2016) 348–355. http://dx.doi.org/10.1016/j.matdes.2016.04.074.

[15] P. Mercelis, J.-P.J. Kruth, Residual stresses in selective laser sintering and selective laser melting, Rapid Prototyp. J. 12 (2006) 254–265. http://dx.doi.org/10.1108/13552540610707013.

[16] M.F. Zaeh, G. Branner, Investigations on residual stresses and deformations in selective laser melting, Prod. Eng. 4 (2010) 35–45. http://dx.doi.org/10.1007/s11740-009-0192-y.

[17] I. Yadroitsava, S. Grewar, D. Hattingh, I. Yadroitsev, Residual Stress in SLM Ti6Al4V Alloy Specimens, Mater. Sci. Forum 828–829 (2015) 305–310. http://dx.doi.org/10.4028/www.scientific.net/MSF.828-829.305.

[18] C. Li, C.H. Fu, Y.B. Guo, F.Z. Fang, A multiscale modeling approach for fast prediction of part distortion in selective laser melting, J. Mater. Process. Technol. 229 (2016) 703–712. http://dx.doi.org/10.1016/j.jmatprotec.2015.10.022.

[19] P. Vora, K. Mumtaz, I. Todd, N. Hopkinson, AlSi12 in-situ alloy formation and residual stress reduction using anchorless selective laser melting, Addit. Manuf. 7 (2015) 12–19. http://dx.doi.org/10.1016/j.addma.2015.06.003.

[20] P. Prabhakar, W.J. Sames, R. Dehoff, S.S. Babu, Computational modeling of residual stress formation during the electron beam melting process for Inconel 718, Addit. Manuf. 7 (2015) 83–91. http://dx.doi.org/10.1016/j.addma.2015.03.003.

[21] L. Parry, I.A. Ashcroft, R.D. Wildman, Understanding the effect of laser scan strategy on residual stress in selective laser melting through thermo-mechanical simulation, Addit. Manuf. 12 (2016) 1–15. http://dx.doi.org/10.1016/j.addma.2016.05.014.

[22] B. Vrancken, R. Wauthle, J. Kruth, J. Van Humbeeck, Study of the Influence of Material Properties on Residual Stress in Selective Laser Melting, in: Proceedings of the 24th International Solid Free. Fabr. Symp 393–407, 2013.

[23] J.C. Heigel, P. Michaleris, E.W. Reutzel, Thermo-mechanical model development and validation of directed energy deposition additive manufacturing of Ti-6Al-4V, Addit. Manuf. 5 (2015) 9–19. http://dx.doi.org/10.1016/j.addma.2014.10.003.

[24] A. Hussein, L. Hao, C. Yan, R. Everson, Finite element simulation of the temperature and stress fields in single layers built without-support in selective laser melting, Mater. Des. 52 (2013) 638–647. http://dx.doi.org/10.1016/j.matdes.2013.05.070.

[25] A.H. Nickel, D.M. Barnett, F.B. Prinz, Thermal stresses and deposition patterns in layered manufacturing, Mater. Sci. Eng. A. 317 (2001) 59–64. http://dx.doi.org/10.1016/S0921-5093(01)01179-0.

[26] B. Cheng, S. Shrestha, K. Chou, Stress and deformation evaluations of scanning strategy effect in selective laser melting, Addit. Manuf. (2016). http://dx.doi.org/10.1016/j.addma.2016.05.007.

[27] J.-P. Kruth, J. Deckers, E. Yasa, R. Wauthlé, R. Wauthle, Assessing and comparing influencing factors of residual stresses in selective laser melting using a novel analysis method, Proc. Inst. Mech. Eng. Part B J. Eng. Manuf. 226 (2012) 980–991. http://dx.doi.org/10.1177/0954405412437085.

[28] J.P. Kruth, L. Froyen, J. Van Vaerenbergh, P. Mercelis, M. Rombouts, B. Lauwers, Selective laser melting of iron-based powder, J. Mater. Process. Technol. 149 (2004) 616–622. http://dx.doi.org/10.1016/j.jmatprotec.2003.11.051.

[29] L. Thijs, K. Kempen, J.-P. Kruth, J. Van Humbeeck, Fine-structured aluminium products with controllable texture by selective laser melting of pre-alloyed AlSi10Mg powder, Acta Mater. 61 (2013) 1809–1819. http://dx.doi.org/10.1016/j.actamat.2012.11.052.

[30] Y. Lu, S. Wu, Y. Gan, T. Huang, C. Yang, L. Junjie, J. Lin, Study on the microstructure, mechanical property and residual stress of SLM Inconel-718 alloy manufactured by differing island scanning strategy, Opt. Laser Technol. 75 (2015) 197–206. http://dx.doi.org/10.1016/j.optlastec.2015.07.009.

[31] Q. Bo, S. Yu-sheng, W. Qing-song, W. Hai-bo, The helix scan strategy applied to the selective laser melting, Int. J. Adv. Manuf. Technol. 63 (2012) 631–640. http://dx.doi.org/10.1007/s00170-012-3922-9.

[32] D.M. Keicher, W.D. Miller, Multiple beams and nozzles to increase deposition rate, US 5993554 A, 2001.

[33] J.J. Keremes, J.D. Haynes, Y. Gao, D.E. Matejczyk, Laser configuration for additive manufacturing, US 20130112672 A1, 2013.

[34] T.J. Rockstroh, D.C. Gray, M.A. Cheverton, V.P. Ostroverkhov, Selective laser melting additive manufacturing method with simultaneous multiple melting lasers beams and apparatus therefor, WO 2015191257 A1, 2015.

[35] M. Fockele, Device for manufacture of objects by layer-wise constructing from powder-form material has sub-systems of irradiating unit allocated to respective sections of building field on base arrangement, EP1839781 A3, 2006.

[36] M. Masoomi, S.M. Thompson, N. Shamsaei, Quality Part production via multi-laser additive manufacturing, 2017(Submitted for publication).

[37] Y. Lu, S. Wu, Y. Gan, J. Li, C. Zhao, D. Zhuo, J. Lin, Investigation on the microstructure, mechanical property and corrosion behavior of the selective laser melted CoCrW alloy for dental application, Mater. Sci. Eng. C. 49 (2015) 517–525. http://dx.doi.org/10.1016/j.msec.2015.01.023.

[38] A. Wiesner, D. Schwarze, Multi-Laser selective laser melting, in: Proceedings of the 8th International Conference Photonic Technol., Fürth, Germany, 2014.

[39] N.F. Williams, Endoprosthesis having multiple laser welded junctions method and procedure, US 5716396 A, 1998.

[40] Y. Hu, W.F. Hehmann, Multi-laser beam welding high strength superalloys, US 6972390 B2, 2005.

[41] J.A. Benda, A. Parasco, Apparatus for multiple beam laser sintering, US5508489 A, 1996.

[42] I. Gurrappa, Characterization of titanium alloy Ti-6Al-4V for chemical, marine and industrial applications, Mater. Charact. 51 (2003) 131–139. http://dx.doi.org/10.1016/j.matchar.2003.10.006.

[43] L.E. Murr, S.A. Quinones, S.M. Gaytan, M.I. Lopez, A. Rodela, E.Y. Martinez, D.H. Hernandez, E. Martinez, F. Medina, R.B. Wicker, Microstructure and mechanical behavior of Ti-6Al-4V produced by rapid-layer manufacturing, for biomedical applications, J. Mech. Behav. Biomed. Mater. 2 (2009) 20–32. http://dx.doi.org/10.1016/j.jmbbm.2008.05.004.

[44] S.S. Al-Bermani, M.L. Blackmore, W. Zhang, I. Todd, The origin of microstructural diversity, texture, and mechanical properties in electron beam melted Ti-6Al-4V, Metall. Mater. Trans. A. 41 (2010) 3422–3434. http://dx.doi.org/10.1007/s11661-010-0397-x.

[45] Saad A. Khairallah, Andrew T. Anderson, Alexander Rubenchik, Wayne King, Laser powder-bed fusion additive manufacturing: physics of complex melt flow and formation mechanisms of pores, spatter, and denudation zones, Acta Mater. 108 (2016) 36–45. http://dx.doi.org/10.1016/j.actamat.2016.02.014.

[46] Y. Li, D. Gu, Parametric analysis of thermal behavior during selective laser melting additive manufacturing of aluminum alloy powder, Mater. Des. 63 (2014) 856–867. http://dx.doi.org/10.1016/j.matdes.2014.07.006.

[47] B. Valsecchi, B. Previtali, E. Gariboldi, A. Liu, Characterisation of the thermal damage in a martensitic steel substrate consequent to laser cladding process, Procedia Eng. 10 (2011) 2851–2856. http://dx.doi.org/10.1016/j.proeng.2011.04.474.

[48] C.M. Taylor, P.T.H.C. Childs, Thermal Experiments in Direct Metal Laser Sintering, in: Proceedings of the Euro RP, 2001.

[49] Bert Huis in't Veld, L. Overmeyer, M. Schmidt, K. Wegener, A. Malshe, P. Bartolo, Micro additive manufacturing using ultra short laser pulses, CIRP Ann. - Manuf. Technol. 64 (2015) 701–724. http://dx.doi.org/10.1016/j.cirp.2015.05.007.

[50] S.M. Thompson, H.B. Ma, Thermal spreading analysis of rectangular heat spreader, J. Heat. Transf. 136 (2014) 64503. http://dx.doi.org/10.1115/1.4026558.

[51] S.S. Sih, J.W. Barlow, S. Sumin Sih, J.W. Barlow, S.S. Sih, J.W. Barlow, S. Sumin Sih, J.W. Barlow, The prediction of the emissivity and thermal conductivity of powder beds, Part. Sci. Technol. 22 (2004) 291–304. http://dx.doi.org/10.1080/02726350490501682a.

[52] Y.P. Lei, H. Murakawa, Y.W. Shi, X.Y. Li, Numerical analysis of the competitive influence of Marangoni flow and evaporation on heat surface temperature and molten pool shape in laser surface remelting, Comput. Mater. Sci. 21 (2001) 276–290. http://dx.doi.org/10.1016/S0927-0256(01)00143-4.

[53] H. Yin, S.D. Felicelli, L. Wang, Fluid flow, heat and mass transfer in the molten pool

of the LENS process, in: TMS Annu. Meet., New Orleans: pp. 261–270, 2008.
[54] S.W. Churchill, A comprehensive correlating equation for forced convection from flat plates, AIChE J. 22 (1976) 264–268. http://dx.doi.org/10.1002/aic.690220207.
[55] E.R. Denlinger, J. Irwin, P. Michaleris, Thermomechanical modeling of additive manufacturing large parts, J. Manuf. Sci. Eng. 136 (2014) 61007. http://dx.doi.org/10.1115/1.4028669.
[56] I. Yadroitsev, P. Krakhmalev, I. Yadroitsava, Selective laser melting of Ti6Al4V alloy for biomedical applications: temperature monitoring and microstructural evolution, J. Alloy. Compd. 583 (2014) 404–409. http://dx.doi.org/10.1016/j.jallcom.2013.08.183.
[57] A. Neira Arce, Thermal modeling and simulation of electron beam melting for rapid prototyping on Ti6Al4V alloys, North Carolina State University, 2012.
[58] M. Boivineau, C. Cagran, D. Doytier, V. Eyraud, M.H. Nadal, B. Wilthan, G. Pottlacher, Thermophysical properties of solid and liquid Ti-6Al-4V (TA6V) alloy, Int. J. Thermophys. 27 (2006) 507–529. http://dx.doi.org/10.1007/s10765-005-0001-6.
[59] P. Fischer, V. Romano, H.P. Weber, N.P. Karapatis, E. Boillat, R. Glardon, Sintering of commercially pure titanium powder with a Nd:YAG laser source, Acta Mater. 51 (2003) 1651–1662. http://dx.doi.org/10.1016/S1359-6454(02)00567-0.
[60] E.W. Lemmon, R.T. Jacobsen, Viscosity and thermal conductivity equations for nitrogen, oxygen, argon, and air, Int. J. Thermophys. 25 (2004) 21–69. http://dx.doi.org/10.1023/B:IJOT.0000022327.04529.f3.
[61] T. Vilaro, C. Colin, J.D. Bartout, As-fabricated and heat-treated microstructures of the Ti-6Al-4V alloy processed by selective laser melting, Metall. Mater. Trans. A. 42 (2011) 3190–3199. http://dx.doi.org/10.1007/s11661-011-0731-y.
[62] W.E. King, A.T. Anderson, R.M. Ferencz, N.E. Hodge, C. Kamath, S.A. Khairallah, A.M. Rubenchik, Laser powder bed fusion additive manufacturing of metals; physics, computational, and materials challenges, Appl. Phys. Rev. 2 (2015) 41304. http://dx.doi.org/10.1063/1.4937809.
[63] G. Kasperovich, J. Haubrich, J. Gussone, G. Requena, Correlation between porosity and processing parameters in TiAl6V4 produced by selective laser melting, Mater. Des. 105 (2016) 160–170. http://dx.doi.org/10.1016/j.matdes.2016.05.070.
[64] M. Khanzadehdaghalian, L. Bian, N. Shamsaei, S.M. Thompson, Porosity Detection of Laser Based Additive Manufacturing Using Melt Pool Morphology Clustering, in: Solid Free. Fabr. 2016 in: Proceedings of the 26th Annu. International, Austin: pp. 1487–1494, 2016.
[65] C. Qiu, C. Panwisawas, M. Ward, H.C. Basoalto, J.W. Brooks, M.M. Attallah, On the role of melt flow into the surface structure and porosity development during selective laser melting, Acta Mater. 96 (2015) 72–79. http://dx.doi.org/10.1016/j.actamat.2015.06.004.
[66] C. Ho, M. Wen, Distribution of the intensity absorbed by the keyhole wall in laser processing, J. Mater. Process. Technol. 145 (2004) 303–310. http://dx.doi.org/10.1016/j.jmatprotec.2003.07.009.
[67] A.J. Sterling, B. Torries, N. Shamsaei, S.M. Thompson, D.W. Seely, Fatigue behavior and failure mechanisms of direct laser deposited Ti-6Al-4V, Mater. Sci. Eng. A. 655 (2016) 100–112. http://dx.doi.org/10.1016/j.msea.2015.12.026.
[68] B. Torries, A.J. Sterling, N. Shamsaei, S.M. Thompson, S.R. Daniewicz, Utilization of a microstructure sensitive fatigue model for additively manufactured Ti-6Al-4V, Rapid Prototyp. (2016). http://dx.doi.org/10.1108/RPJ-11-2015-0168.
[69] B. Torries, S. Shao, N. Shamsaei, S.M. Thompson, Effect of Inter-Layer Time Interval on the Mechanical Behavior of Direct Laser Deposited Ti-6Al-4V, in: Solid Free. Fabr. 2016 Proceedings 26th Annu. International, Austin: pp. 175–184, 2016.
[70] H. Galarraga, D.A. Lados, R.R. Dehoff, M.M. Kirka, P. Nandwana, Effects of the microstructure and porosity on properties of Ti-6Al-4V ELI alloy fabricated by electron beam melting (EBM), Addit. Manuf. 10 (2016) 47–57. http://dx.doi.org/10.1016/j.addma.2016.02.003.
[71] A. Yadollahi, N. Shamsaei, S.M. Thompson, A. Elwany, L. Bian, Effects of building orientation and heat treatment on fatigue behavior of selective laser melted 17-4 PH stainless steel, Int. J. Fatigue 94 (2017) 218–235. http://dx.doi.org/10.1016/j.ijfatigue.2016.03.014.
[72] L. Thijs, F. Verhaeghe, T. Craeghs, J. Van Humbeeck, J.P. Kruth, A study of the microstructural evolution during selective laser melting of Ti-6Al-4V, Acta Mater. 58 (2010) 3303–3312. http://dx.doi.org/10.1016/j.actamat.2010.02.004.
[73] W. Xu, E.W. Lui, A. Pateras, M. Qian, M. Brandt, In situ tailoring microstructure in additively manufactured Ti-6Al-4V for superior mechanical performance, Acta Mater. 125 (2017) 390–400. http://dx.doi.org/10.1016/j.actamat.2016.12.027.
[74] B. Song, S. Dong, B. Zhang, H. Liao, C. Coddet, Effects of processing parameters on microstructure and mechanical property of selective laser melted Ti6Al4V, Mater. Des. 35 (2012) 120–125. http://dx.doi.org/10.1016/j.matdes.2011.09.051.
[75] S.M. Kelly, S.L. Kampe, Microstructural evolution in laser-deposited multilayer Ti-6Al-4V builds: Part II. thermal modeling, Metall. Mater. Trans. A. 35 (2004) 1861–1867. http://dx.doi.org/10.1007/s11661-004-0094-8.
[76] R. Paul, S. Anand, F. Gerner, Effect of Thermal Deformation on Part Errors in Metal Powder Based Additive Manufacturing Processes, J. Manuf. Sci. Eng. 136 (2014) 31009. http://dx.doi.org/10.1115/1.4026524.
[77] P. Edwards, M. Ramulu, Fatigue performance evaluation of selective laser melted Ti-6Al-4V, Mater. Sci. Eng. A. 598 (2014) 327–337. http://dx.doi.org/10.1016/j.msea.2014.01.041.